Cell Reports

Article

Restriction factor screening identifies RABGAP1L-mediated disruption of endocytosis as a host antiviral defense

Graphical abstract

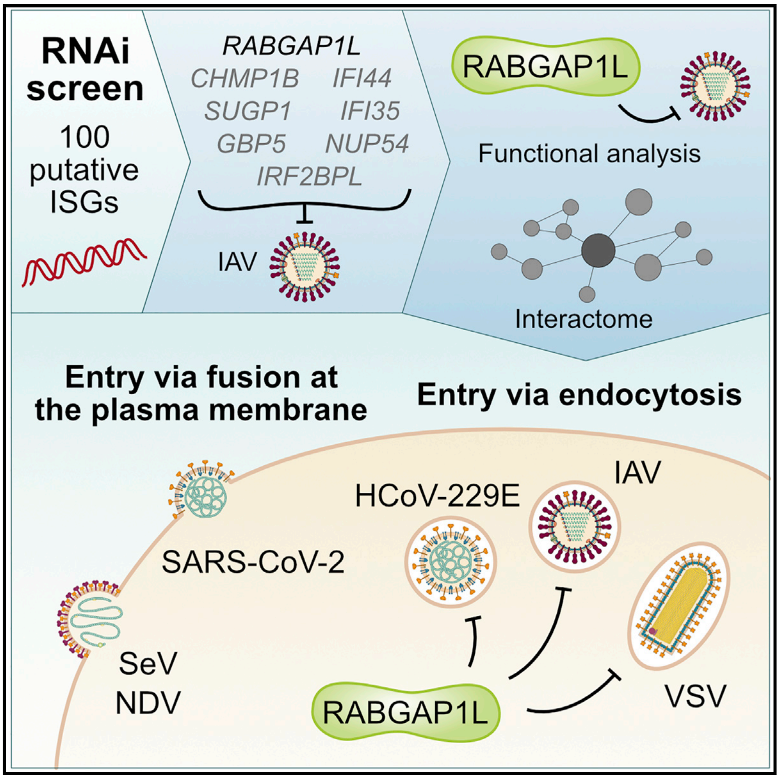

Authors

Sonja Fernbach, Eva E. Spieler, Idoia Busnadiego, Umut Karakus, Anouk Lkharrazi, Silke Stertz, Benjamin G. Hale

Correspondence

hale.ben@virology.uzh.ch

In brief

Interferons inhibit viruses through the concerted action of many host restriction factors. Here, Fernbach et al. use siRNA screening to identify interferon-dependent host factors that limit early stages of the influenza A virus replication cycle, leading to the characterization of RABGAP1L-mediated disruption of endocytosis as a broadly acting host antiviral mechanism.

Highlights

- An siRNA screen identifies genes contributing to the antiviral action of interferon
- RABGAP1L potentiates the action of interferon against multiple RNA viruses
- The RABGAP1L proximal interactome reveals its association with endosomal proteins
- RABGAP1L disrupts endocytosis to limit cell entry of viruses using this pathway

Fernbach et al., 2022, Cell Reports *38*, 110549
March 22, 2022 © 2022 The Author(s).
https://doi.org/10.1016/j.celrep.2022.110549

CellPress

Cell Reports

CellPress
OPEN ACCESS

Article

Restriction factor screening identifies RABGAP1L-mediated disruption of endocytosis as a host antiviral defense

Sonja Fernbach,[1,2] Eva E. Spieler,[1,2] Idoia Busnadiego,[1,3] Umut Karakus,[1,3] Anouk Lkharrazi,[1,3] Silke Stertz,[1] and Benjamin G. Hale[1,4,*]
[1]Institute of Medical Virology, University of Zurich, 8057 Zurich, Switzerland
[2]Life Science Zurich Graduate School, ETH and University of Zurich, 8057 Zurich, Switzerland
[3]These authors contributed equally
[4]Lead contact
*Correspondence: hale.ben@virology.uzh.ch
https://doi.org/10.1016/j.celrep.2022.110549

SUMMARY

Host interferons (IFNs) powerfully restrict viruses through the action of several hundred IFN-stimulated gene (ISG) products, many of which remain uncharacterized. Here, using RNAi screening, we identify several ISG restriction factors with previously undescribed contributions to IFN-mediated defense. Notably, RABGAP1L, a Tre2/Bub2/Cdc16 (TBC)-domain-containing protein involved in regulation of small membrane-bound GTPases, robustly potentiates IFN action against influenza A viruses (IAVs). Functional studies reveal that the catalytically active TBC domain of RABGAP1L promotes antiviral activity, and the RABGAP1L proximal interactome uncovered its association with proteins involved in endosomal sorting, maturation, and trafficking. In this regard, RABGAP1L overexpression is sufficient to disrupt endosomal function during IAV infection and restricts an early post-attachment, but pre-fusion, stage of IAV cell entry. Other RNA viruses that enter cells primarily via endocytosis are also impaired by RABGAP1L, while entry promiscuous SARS-CoV-2 is resistant. Our data highlight virus endocytosis as a key target for host defenses.

INTRODUCTION

Entry into a host cell is one of the first processes that viruses must achieve for successful infection and highlights a complex interplay between virus particles, co-opted cellular factors, and host defense mechanisms. Influenza A virus (IAV) entry is mediated by its glycoprotein hemagglutinin (HA), which binds to the receptor sialic acid on the surface of cells and triggers internalization of the virus by endocytosis or, less frequently, by macropinocytosis. Subsequent maturation of early to late endosomes, and their acidification, facilitates HA-mediated fusion between viral and host endosomal membranes, resulting in the release of viral genomes into the cytoplasm prior to their transport into the nucleus where replication occurs (Krammer et al., 2018; Long et al., 2019; Sempere Borau and Stertz, 2021).

The critical and early nature of virus entry into the cell makes it a prime target for host defense mechanisms to act swiftly to limit infection. In this regard, several interferon (IFN)-stimulated gene (ISG) products, key effectors of the innate immune IFN system (Schoggins, 2019), have previously been described to impair IAV entry at various stages (Iwasaki and Pillai, 2014). For example, IFITM3 is an IFN-inducible transmembrane protein that localizes to late endosomes/lysosomes and blocks membrane fusion of viruses that enter cells via endocytosis (Brass et al., 2009; Desai et al., 2014). Furthermore, a short isoform of NCOA7 is a recently identified ISG product that promotes vesicle acidification, lysosomal protease activity, and the degradation of endocytosed material, thereby also limiting entry of viruses such as IAV (Doyle et al., 2018). With respect to other viruses, IFN-mediated control of virus entry is also a key host defense, with proteins such as LY6E, which has been shown to restrict several coronaviruses (including severe acute respiratory syndrome coronavirus 2 [SARS-CoV-2]), inhibiting fusion between viral and cellular membranes (Pfaender et al., 2020; Zhao et al., 2020). Surprisingly, a previous study has linked LY6E to promoting IAV infection by stimulating viral uncoating (Mar et al., 2018), suggesting that some ISG products exert differential functions depending on the virus. Indeed, some ISG products appear to have been repurposed by viruses to benefit their replication (Schoggins et al., 2011; Tran et al., 2020).

In this study, we sought to identify previously unknown host restriction factors that limit IAV replication in response to IFN stimulation. Previous screens that have attempted to discover such anti-IAV factors have mostly focused on overexpression-based approaches and have generally assayed the impact of individual ISG products in the absence of either IFN or other ISGs (Kane et al., 2016; Kuroda et al., 2020; Liu et al., 2012; Schoggins et al., 2011, 2014; Wilson et al., 2012). Nevertheless, such screens have proved to be incredibly important and have led to the identification of several previously unappreciated antivirally active ISG products such as CNP, TAP1, IDO1, and TRIM56 (Kane et al., 2016; Liu et al., 2012; Schoggins et al., 2014; Wilson et al., 2012). As an orthogonal approach, we undertook a targeted small interfering RNA (siRNA)-based depletion screen of 100 putative ISGs with the aim of identifying host restriction factors that may function efficiently only in the context of an IFN response. A prominent hit from our screen was RAB GTPase-activating protein 1-like (RABGAP1L), also known as TBC1D18, a member of the Tre2/Bub2/Cdc16 (TBC)-domain-containing protein family, which is involved in the regulation of small membrane-bound GTPases, so-called RAB proteins (Frasa et al., 2012). We found that overexpression of RABGAP1L potentiated the antiviral action of IFN against a panel of viruses, including IAV, and that its function required a catalytically active TBC domain. A validated proximity-labeling proteomic approach revealed the host interactome of RABGAP1L, identifying components of endosomal sorting, maturation, and trafficking pathways. Consistent with this, infection-stage mapping assays uncovered that RABGAP1L expression appears to disrupt endosomal function and limits IAV entry at or prior to virus-host membrane fusion. Thus, our work identifies and characterizes a host factor that can act to limit an early event of the virus infection process.

RESULTS

RNAi screening identifies putative ISGs that restrict early events in the IAV replication cycle

We established a customized siRNA library targeting a subset of human genes that have been described as ISGs in various studies but which mostly have yet to be implicated as antiviral against IAV. The library comprises a total of 403 siRNAs, with 4 siRNAs targeting each of the 100 putative ISGs selected, single validated siRNAs targeting the known anti-IAV ISGs *MX1* and *IFITM3* (positive controls), and a scrambled non-targeting (NT) siRNA (negative control) (Table S1). To identify putative ISG products with antiviral action against IAV, each siRNA from this library was transfected into a modified primary-like human lung fibroblast cell line, MRC-5-HA, for 30 h prior to stimulation of cells with 1,000 U/mL of IFNα2 for 16 h. Cells were then infected with WSN/33-*Renilla* IAV (Spieler et al., 2020) at an MOI of 5 PFU/cell, and *Renilla* luciferase activity was monitored in live cells over the course of 12 h as a surrogate measure for single-cycle viral replication (Figures 1A and 1B). Confirming the setup of our screening assay, in NT siRNA-transfected cells, IFNα2-treatment reduced WSN/33-*Renilla* IAV replication approximately 100-fold, while in *MX1* and *IFITM3* siRNA-transfected cells, the antiviral effects of IFNα2 were notably reduced (Figure 1C). We derived area under the curve (AUC) values of viral replication between 3 and 12 h post-infection following IFNα2 treatment and calculated *Z* scores for each target siRNA relative to multiple NT siRNA replicates that were included in the screen. From the 100 putative ISGs targeted in this primary screen, 22 met our stringent criteria for further consideration (at least 3 out of 4 independent siRNAs had a *Z* score ≥ 2) (Figures 1D; Table S1). By rescreening 20 putative ISGs in a second assay, we were able to confirm that 8 of them, in addition to *MX1* and *IFITM3*, contributed to the antiviral action of IFNα2 against WSN/33-*Renilla* IAV (Figures 1D and 1E; Table S1). Interestingly, these included genes such as *GBP5* and *IFI44*, which were independently validated by others as antiviral ISG products during the course of our study (Braun et al., 2019; Busse et al., 2020). These observations support the robustness of our screening efforts and provide confidence in our identification of several putative ISG products that contribute to the antiviral function of IFNα2 against early stages of the IAV replication cycle.

RABGAP1L expression restricts IAV

We focused follow-up studies on *RABGAP1L*, which ranked highest in our RNAi screens and which encodes RABGAP1L, a member of the TBC-domain-containing protein family that is involved in the regulation of small membrane-bound GTPases (Frasa et al., 2012). To further validate RABGAP1L as a factor restricting IAV, we transfected A549 cells with a panel of 5 different siRNAs targeting *RABGAP1L* and assessed the antiviral action of IFNα2 against WSN/33-*Renilla* IAV. None of the 5 *RABGAP1L* siRNAs impacted general cell viability (Figure 2A). However, 4 of the 5 *RABGAP1L* siRNAs led to a statistically significant reduction in the ability of IFNα2 to limit IAV replication, although none were as effective as an siRNA targeting the essential ISG transcription factor *IRF9* (Figures 2B and 2C). In line with this, western-blot analysis revealed that RABGAP1L depletion does not limit general ISG induction by IFNα2 (as evidenced by IFNα2-induced MxA protein levels) (Figure 2D). Surprisingly, despite reports of *RABGAP1L* mRNA induction by IFNα and IFNγ in primary hepatocytes (He et al., 2010), we did not observe IFN-mediated induction of RABGAP1L in MRC5 or A549 cells, nor in a diverse panel of other human cells, either at the mRNA or protein levels (Figures S1A–S1D).

Of the multiple putative RABGAP1L isoforms annotated (NCBI: 9910), our western blot analysis identified four that matched to the predicted molecular masses of isoforms A, G, H, and I (Figures 2D and 2E). To validate the results of our siRNA experiments, we therefore took an orthogonal approach and generated A549 cells stably overexpressing each of these four isoforms individually to assess their impact on IFN-mediated antiviral activity. We confirmed similar expression of the RABGAP1L isoforms between the different cell lines by both western blot and immunofluorescence analyses (Figures 2F and 2G). In line with the siRNA data, overexpression of each RABGAP1L isoform slightly limited the replication of WSN/33-*Renilla* IAV, as well as wild-type WSN/33 IAV, in unstimulated cells, but strongly potentiated antiviral activity in IFNα2-stimulated cells (Figures 2H, S2A, and S2B). Notably, the shorter RABGAP1L isoforms, A and H, which lack C-terminal extensions, exhibited the strongest IFN-dependent antiviral effects. Consistent with our siRNA-based experiments, overexpression of the main RABGAP1L isoform A did not appear to influence the IFN signaling response or general ISG induction by IFNα2 (Figures S2C–S2E). Thus, independent siRNA and overexpression data indicate that RABGAP1L can restrict IAV. While RABGAP1L does not appear to be a universal ISG product, or to regulate general ISG expression, our results suggest that RABGAP1L functions in concert with IFN stimulation to limit IAV replication.

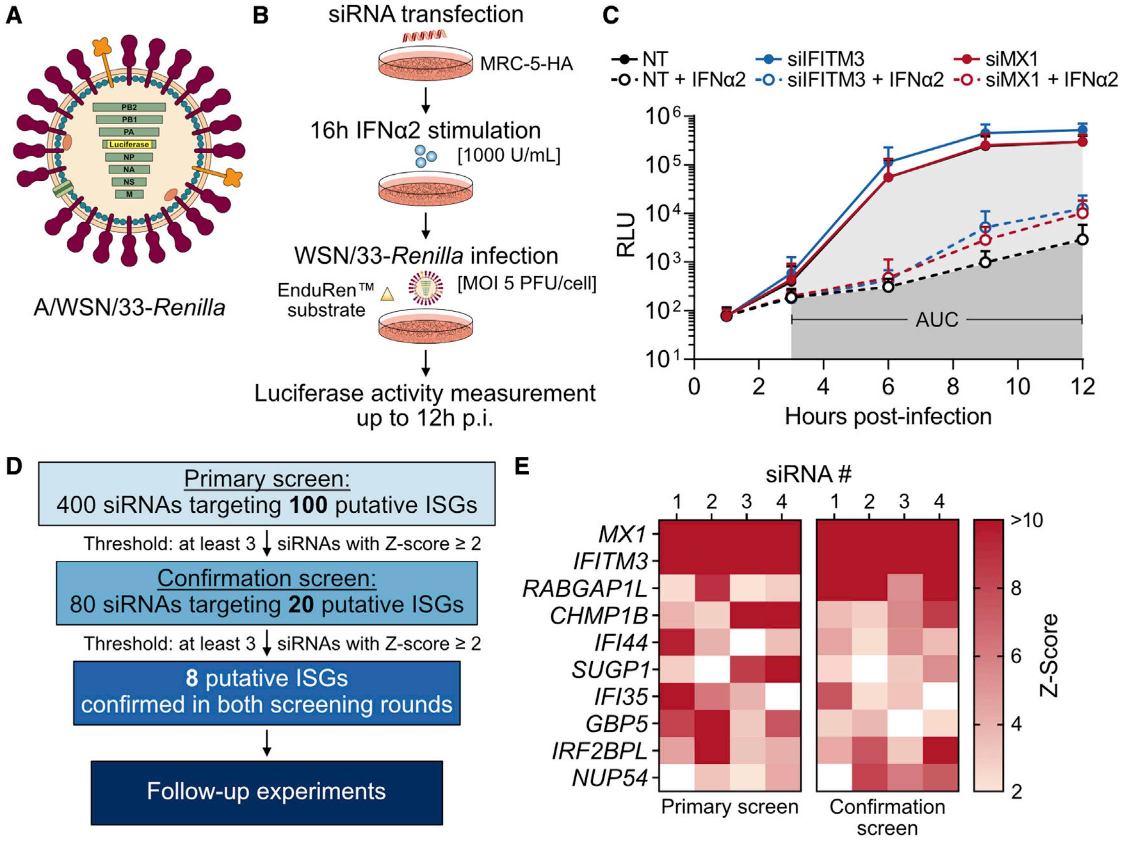

Figure 1. RNAi screening identifies RABGAP1L as an IAV restriction factor

(A) Schematic representation of recombinant IAV WSN/33 in which the coding region for the hemagglutinin (HA) glycoprotein has been replaced by *Renilla* luciferase (WSN/33-*Renilla*).

(B) RNAi-screening experimental workflow.

(C) MRC-5-HA cells were transfected for 30 h with individual siRNAs targeting *MX1* or *IFITM3* or with a non-targeting (NT) control siRNA. Following stimulation with IFNα2 (1,000 U/mL or mock) for 16 h, cells were infected with WSN/33-*Renilla* (MOI 5 PFU/cell) in the presence of the live-cell substrate EnduRen. Luciferase activity was monitored up to 12 h post-infection (p.i.), and the area under the curve (AUC) was calculated as indicated. Mean values from 50 technical replicates across two independent biological experiments are plotted, with error bars representing SDs.

(D) Hit criteria for RNAi screening. In a primary screen following the workflow in (B), 100 putative ISGs were silenced with four individual siRNAs each. Twenty-two genes met the threshold, and 20 were re-tested in a confirmation screen. Applying the same hit criteria, a total of 8 putative ISGs were confirmed in both screening rounds.

(E) Heatmap showing *Z* scores of positive controls (*MX1* and *IFITM3*) and the top 8 hits from the two RNAi-screening rounds. Columns represent individual siRNAs targeting genes listed in rows.

See also Table S1.

RABGAP1L overexpression restricts selected positive- and negative-sense RNA viruses

We used RABGAP1L isoform A (from now on simply referred to as RABGAP1L) as a basis for further work given that it exerted strong antiviral activity and appeared to be the dominantly expressed isoform in most cell types tested (Figure S1D). Stable RABGAP1L overexpression in A549 cells potentiated IFNα2-mediated restriction not only of WSN/33 IAV but also of *Renilla* luciferase reporter variants of human pandemic A/Netherlands/602/09 (pdmH1N1) IAV and the A/Vietnam/1203/04 (H5N1) IAV (Figure 3A). Notably, pdmH1N1 IAV replication was also strongly inhibited by RABGAP1L overexpression in the absence of IFNα2. To examine the antiviral potential of RABGAP1L against other viruses in different cell types, we also generated Huh-7, Calu-3, and Vero-CCL81 cells stably overexpressing RABGAP1L or GFP as a control. RABGAP1L overexpression led to a reduction in WSN/33-*Renilla* IAV replication in A549, Huh-7, Calu-3, and Vero-CCL81 cell lines (Figures 3A–3H). Furthermore, it was clear that both a *Renilla*-encoding human coronavirus (HCoV-229E-*Renilla*) and a GFP-encoding vesicular stomatitis virus (VSV-GFP) were also limited in their replication capacities in cells overexpressing RABGAP1L (Figures 3B and 3C). Notably, HCoV-229E-*Renilla* did not seem particularly sensitive to IFNα2 pre-treatment but was inhibited by RABGAP1L overexpression alone (Figure 3B). This contrasted with the effects of RABGAP1L on VSV-GFP replication, where overexpression of RABGAP1L alone had a small effect on virus replication but was strongly potentiated by IFNα2 (Figure 3C). Strikingly, we did not observe an inhibitory effect of RABGAP1L overexpression on replication of two GFP-encoding paramyxoviruses,

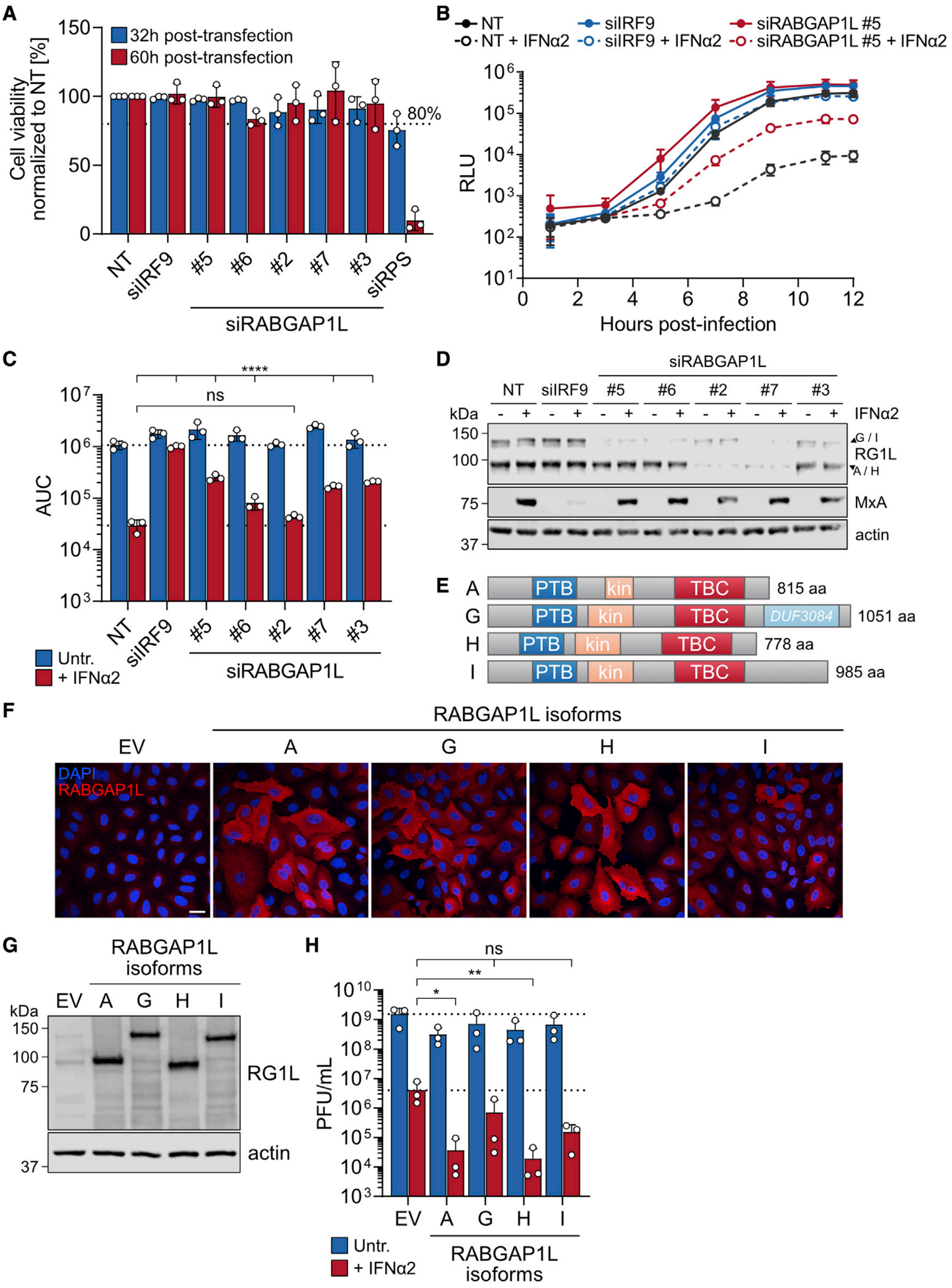

Figure 2. IFN-mediated restriction of IAV by RABGAP1L

(A) A549 cells were transfected with the indicated siRNAs for 32 or 60 h prior to lysis and assessment of cell viability using CellTiter-Glo. An NT siRNA and an siRNA targeting *IRF9* were used as negative controls. siRPS is an siRNA targeting the essential gene *RPS27A* and thus acted as a positive control for cell toxicity. Mean values from three biologically independent experiments are plotted, with error bars representing SDs. Individual data points are shown.

(legend continued on next page)

Sendai virus (SeV-GFP) or Newcastle disease virus (NDV-GFP), in A549 cells (Figures 3D and 3E). Nor did we observe an inhibitory effect of RABGAP1L overexpression on replication of SARS-CoV-2 in either Calu-3 or Vero-CCL81 cells (Figures 3G and 3I). Together, these data show that RABGAP1L overexpression can restrict the replication of different RNA viruses beyond IAV. For most of the tested viruses, RABGAP1L-mediated restriction is potentiated by IFNα2, although RABGAP1L overexpression alone can limit the replication of some viruses, in some cell lines, in the absence of IFNα2 (e.g., pdmH1N1 IAV and HCoV-229E). However, some other RNA viruses, such as SARS-CoV-2 and the tested paramyxoviruses, appear to be resistant to the inhibitory effect of RABGAP1L.

The antiviral function of RABGAP1L relies on its catalytically active TBC domain and residues implicated in endosomal trafficking

RABGAP1L contains three described domains: an N-terminal phosphotyrosine-binding (PTB) domain, a kinesin-like domain, and a C-terminal TBC domain, which regulates small membrane-bound GTPases (Figure 4A). To explore the functionality of RABGAP1L, we generated a panel of C-terminal deletions in RABGAP1L and screened them for antiviral activity following production of stably expressing A549-based cell lines (Figures 4A and S3A). Western blot and immunofluorescence analyses revealed that all the truncation constructs exhibited similar intracellular localization patterns to full-length RABGAP1L, and all appeared to express homogeneously in cells, even if total protein abundance differed slightly between some constructs (Figures 4B, S3B, and S3C). Importantly, no apparent cell growth defect was detected in cells expressing RABGAP1L or its different truncated variants (Figure S3D). Compared with full-length RABGAP1L, we noted that deletion of only the TBC domain (ΔTBC) led to a clear reduction in the ability of RABGAP1L to restrict IAV replication following IFNα2 pre-treatment (Figures S3E and S3F). However, given the poor expression of this construct, we focused on a RABGAP1L mutant that appeared to be more stable (termed 421) and which lacked both the TBC domain and the region between the kinesin-like and the TBC domains. Compared with full-length RABGAP1L, the RABGAP1L-421 truncation mutant exhibited no antiviral activity against WSN/33 IAV replication following IFNα2 pre-treatment, underscoring the importance of these domains for RABGAP1L function (Figures 4C, S3E, and S3F).

To further dissect the contributions of the TBC domain to RABGAP1L function, we undertook a targeted mutagenesis approach. Most TBC domains of RABGAP proteins catalyze the GTP hydrolysis of RAB proteins by a dual-finger mechanism, relying on two catalytic arginine (R) and glutamine (Q) residues (Pan et al., 2006). A previous sequence alignment of TBC-domain catalytic regions located the dual-finger motif of RABGAP1L at positions R584 and Q621 (Frasa et al., 2012). As substitution of such residues for alanine (A) in other TBC-domain-containing proteins decrease catalytic efficiency by 100 to 1,000-fold (Pan et al., 2006), we generated RABGAP1L constructs with the R584A (R_{mut}), Q621A (Q_{mut}), or double (RQ_{mut}) substitutions to assay whether they abrogated the antiviral activity of RABGAP1L (Figure 4D). In addition, we generated a RABGAP1L KK784EE (KK_{mut}) double substitution construct that is reported to disrupt the interaction of RABGAP1L with Ankyrin B (AnkB) and thereby impact its endosomal trafficking (Qu et al., 2016) (Figure 4D). Following production of stably expressing A549-based cell lines, equal expression of each RABGAP1L construct was ensured by immunofluorescence and western blot analyses (Figures 4E and 4F). Notably, compared with wild type (WT), all the mutant RABGAP1L constructs exhibited reduced antiviral activity against IAV replication following IFNα2 pre-treatment, with both the R_{mut} and RQ_{mut} constructs being particularly ineffective (Figure 4G). Overall, these data reveal that the antiviral activity of RABGAP1L against IAV relies on its catalytically active TBC domain, as well as a likely dependence on endosomal trafficking.

Proximity-labeling-based proteomics identifies the RABGAP1L host interactome

To understand more about the function of RABGAP1L, we determined its human protein interactome in living cells using a previously developed proximity-labeling (PL) approach based on

---

(B and C) A549 cells were transfected with the indicated siRNAs 30 h prior to IFNα2 treatment (1,000 U/mL or mock). Sixteen hours post-IFN stimulation, cells were infected with WSN/33-*Renilla* (MOI 1 PFU/cell), and luciferase activity was monitored every 2 h for a total of 12 h. The NT siRNA and siRNA targeting *IRF9* were used as controls.

(C) The AUC was calculated from measured relative light units (RLUs) over time. Mean values from three biologically independent experiments are plotted, with error bars representing SDs. Individual data points are shown.

(D) In parallel to (B) and (C), cells were harvested for western blot analysis 16 h post-IFN stimulation. Proteins of interest were detected as indicated. RABGAP1L (RG1L) isoforms corresponding to detected bands are highlighted.

(E) Schematic representation of RABGAP1L isoforms A, G, H, and I, showing the phosphotyrosine-binding (PTB) domain, the kinesin-like (kin) domain, and the Tre-2/Bub2/Cdc16 (TBC) domain. Isoform G further contains a domain of unknown function (DUF3084).

(F) Immunofluorescence analysis of A549 cells stably expressing either empty vector (EV) or RABGAP1L isoforms A, G, H, and I. Cells were fixed and stained for RABGAP1L (red); nuclei were stained with DAPI (blue). Scale bar represents 25 μm. Representative confocal-microscopy images from at least two biologically independent experiments are shown.

(G) Cells described in (F) were harvested for western-blot analysis. Proteins of interest were detected with the indicated antibodies. Images are representative of three biologically independent experiments.

(H) Cells described in (F) and (G) were treated with IFNα2 (1,000 U/mL or mock) 16 h prior to infection with WSN/33 (MOI 0.001 PFU/cell). Supernatants were collected 48 h p.i. and titrated on Madin-Darby canine kidney (MDCK) cells to determine viral titers. Mean values from three biologically independent experiments are plotted, with error bars representing SDs. Individual data points are shown.

Statistical significance in (C) and (H) was determined using one-way ANOVA following log transformation (*$p < 0.05$, **$p < 0.002$, ****$p < 0.0001$; ns, nonsignificant).

See also Figures S1 and S2.

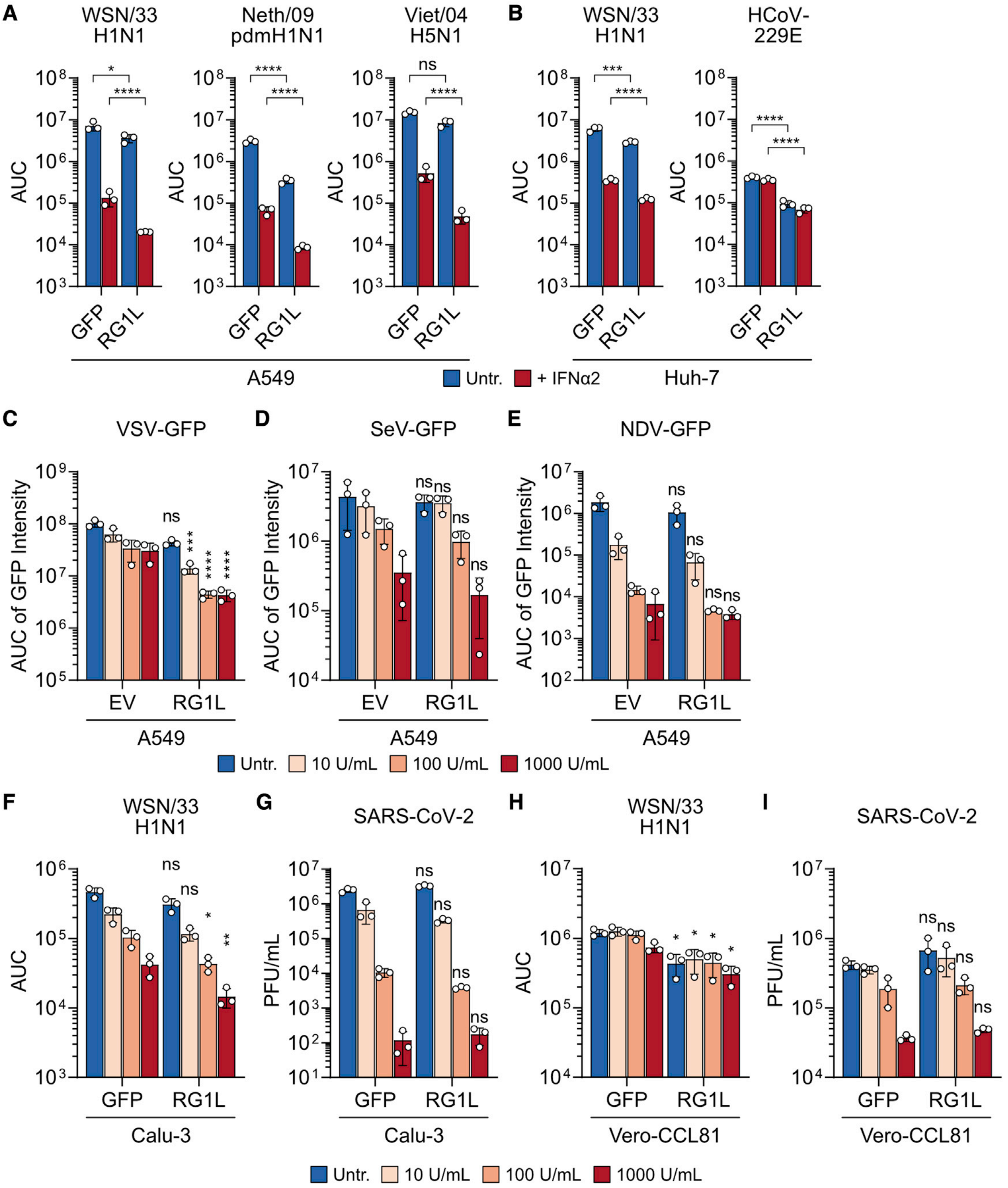

Figure 3. RABGAP1L overexpression restricts selected positive- and negative-sense RNA viruses

(A) A549 cells stably expressing GFP or RABGAP1L (RG1L) were stimulated with IFNα2 (1,000 U/mL or mock) 16 h prior to infection with different *Renilla* luciferase-encoding IAVs: H1N1 (WSN/33, MOI 1 PFU/cell), pdmH1N1 (Neth/09, MOI 5 PFU/cell), or H5N1 (Viet/04, MOI 0.5 PFU/cell). EnduRen live-cell substrate was added p.i., and the luciferase activity was monitored every 2 h for a total of 11 h. The AUC was calculated from RLUs up to 11 h p.i.

(B) Huh-7 cells stably expressing GFP or RG1L were treated as described in (A) and infected with WSN/33-*Renilla* (MOI 1 PFU/cell) or HCoV-229E-*Renilla* (MOI 5 PFU/cell). EnduRen was supplemented, and the luciferase activity was measured every 2 h for a total of 11 h. RLUs were used to calculate the AUC.

(C–E) A549 cells expressing EV or RG1L were stimulated with IFNα2 (10, 100 or 1,000 U/mL or mock) for 4 h prior to infection with VSV-GFP (MOI 1 PFU/cell) (C) or for 16 h prior to infection with SeV-GFP (MOI ~1 PFU/cell) (D) and NDV-GFP (MOI 1 PFU/cell) (E). GFP intensity was measured every 2 h for up to 72 h. The AUC was calculated from total green integrated intensity.

(F and H) Calu-3 (F) or Vero-CCL81 (H) cells stably expressing GFP or RG1L were treated with IFNα2 (10, 100, or 1,000 U/mL or mock) for 16 h, followed by infection with WSN/33-*Renilla* (MOI 1 PFU/cell). EnduRen was added p.i., and the luciferase activity was monitored every 2 h for a total of 11 h. The AUC was calculated from RLUs.

(legend continued on next page)

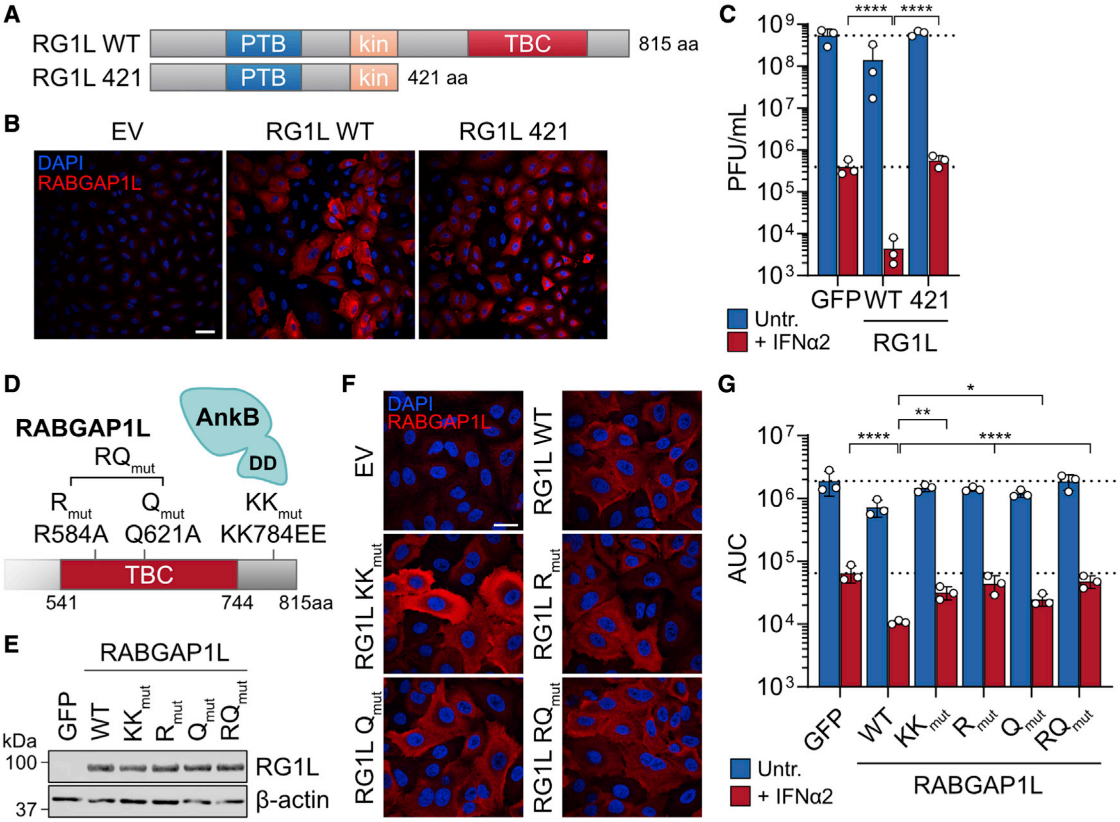

Figure 4. The antiviral function of RABGAP1L relies on its catalytically active TBC domain and residues implicated in endosomal trafficking

(A) Schematic representation of RG1L WT and the 421 mutant (RG1L 421) which lacks the C-terminal region downstream of the kin domain.

(B) Immunofluorescence analysis of A549 cells stably expressing EV, RG1L WT, or RG1L 421. Cells were fixed and stained with the indicated antibodies. Scale bar represents 25 μm.

(C) A549 cells stably expressing GFP, RG1L WT, or RG1L 421 were stimulated with IFNα2 (1,000 U/mL or mock) for 16 h prior to infection with WSN/33 (MOI 0.001 PFU/cell). Supernatants were collected after 48 h and titrated on MDCK cells.

(D) Schematic representation of the TBC domain of RABGAP1L and the localization of mutants R584A (R_{mut}), Q621A (Q_{mut}), R584A-Q621A (RQ_{mut}), and KK784EE (KK_{mut}). KK_{mut} has previously been shown to prevent interaction with the AnkB death domain (DD).

(E) Western blot validation of RABGAP1L expression in A549 cells stably expressing RG1L WT or the indicated mutants.

(F) Immunofluorescence analysis of cells described in (E) (here, EV was used as a control), fixed and stained with the indicated antibodies. Scale bar represents 25 μm.

(G) Cells described in (E) were infected with WSN/33-*Renilla* (MOI 1 PFU/cell) following treatment with IFNα2 (1,000 U/mL or mock) for 16 h. The AUC was calculated from RLU values taken up to 11 h p.i.

For (B), (E), and (F), representative data from three biologically independent experiments are shown. For (C) and (G), mean values from three biologically independent experiments are plotted, with error bars representing SDs. Individual data points are shown. Statistical significance was determined using one-way ANOVA following log transformation (*$p < 0.05$, **$p < 0.002$, ****$p < 0.0001$).

See also Figure S3.

TurboID (Borold et al., 2021; Cho et al., 2020). To this end, we generated TurboID-V5-tagged full-length RABGAP1L (T-V5-RG1L), as well as a TurboID-V5-tagged GFP-nuclear export sequence (NES; T-V5-GFP-NES) fusion construct to act as a negative control (Figure 5A). Following stable expression of each construct in A549 cells, we validated their levels and intracellular localization using western blot and immunofluorescence, confirming their similar and homogeneous expression (Figures 5B and 5C). In addition, we verified that the TurboID-V5-tagged RABGAP1L construct maintained its antiviral action against IAV in the presence of IFNα2 (Figure 5D). To determine RABGAP1L interaction partners in the presence and absence of IFNα2,

---

(G and I) Calu-3 (G) or Vero-CCL81 (I) cells stably expressing GFP or RG1L were treated as described in (F) prior to infection with SARS-CoV-2 (MOI 0.1 PFU/cell). Supernatants were collected 24 h p.i., and viral titers were determined by plaque assay in Vero-E6 cells.

(A–I) Mean values from three biologically independent experiments are plotted, with error bars representing SDs. Individual data points are shown. Statistical significance was determined comparing GFP-overexpressing with RG1L-overexpressing cells in equal treatment conditions in all panels using one-way ANOVA following log transformation (*$p < 0.05$, **$p < 0.002$, ***$p < 0.0002$, ****$p < 0.0001$; ns, non-significant).

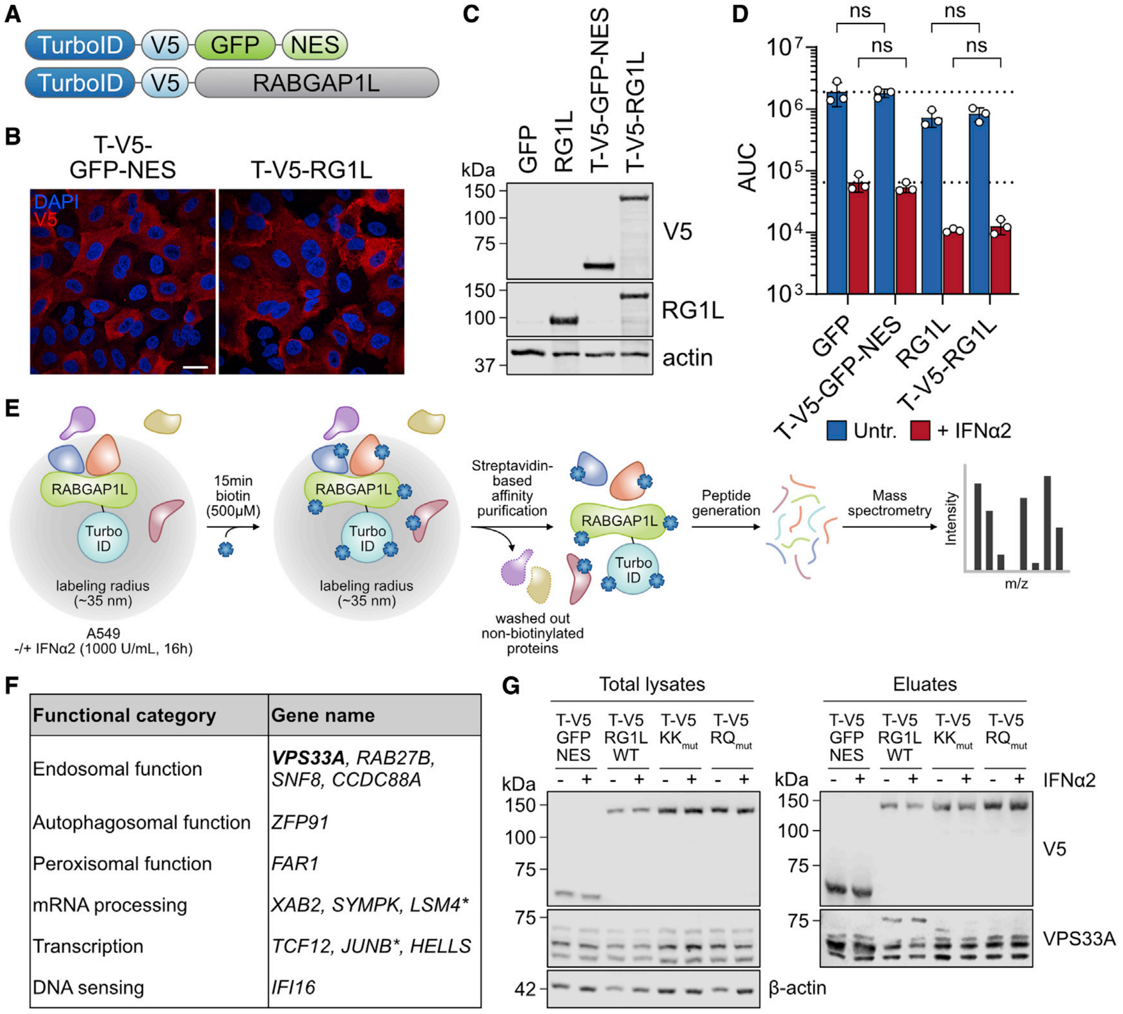

Functional category	Gene name
Endosomal function	***VPS33A***, *RAB27B, SNF8, CCDC88A*
Autophagosomal function	*ZFP91*
Peroxisomal function	*FAR1*
mRNA processing	*XAB2, SYMPK, LSM4**
Transcription	*TCF12, JUNB*, HELLS*
DNA sensing	*IFI16*

Figure 5. Proximity-labeling-based proteomics identifies the RABGAP1L host interactome

(A) Schematic representation of TurboID-V5-tagged (T-V5) GFP (negative control) carrying a nuclear-export sequence (NES) or T-V5-tagged RABGAP1L (T-V5-RG1L).

(B) Constructs described in (A) were stably expressed in A549 cells, and their expression was validated by immunofluorescence using an α-V5 (red) antibody. Nuclei were stained with DAPI (blue). Scale bar represents 25 μm.

(C) Western blot analysis of cells described in (B) compared with A549 cells stably expressing untagged GFP or RABGAP1L (RG1L). Proteins of interest were detected with the indicated antibodies.

(D) Cells described in (C) were stimulated with IFNα2 (1,000 U/mL or mock) 16 h prior to infection with WSN/33-*Renilla* (MOI 1 PFU/cell). The AUC was calculated from RLU values taken up to 11 h p.i. Mean values from three biologically independent experiments are plotted, with error bars representing SDs. Individual data points are shown.

(E) Workflow of the TurboID proximity-labeling approach. Cells described in (B) were treated with IFNα2 (1,000 U/mL or mock) for 16 h, followed by treatment with biotin (500 μM) for 15 min. Following streptavidin-based affinity purification, peptides were generated and subjected to mass-spectrometry analyses.

(F) Interactors specific to RABGAP1L (as compared to GFP-NES) identified using the protocol described in (E). Hits are listed with their gene names and sorted according to previously described functions. Most hits were identified in non-IFNα2-treated samples. Hits marked with an asterisk (*) were identified in the presence and absence of IFNα2, and hits marked in bold were only identified in IFNα2-treated samples.

(G) A549 cells stably expressing constructs introduced in (A) or T-V5-tagged RABGAP1L KK$_{mut}$ and RQ$_{mut}$ were subjected to the proximity labeling approach outlined in (E). Following streptavidin-based affinity purification (samples termed "eluates"), total lysates and eluates were analyzed by western blot. Proteins were detected with the indicated antibodies.

Data obtained in (B), (C), and (G) are representative of three biologically independent experiments. For (D), statistical significance was determined using one-way ANOVA following log transformation (ns, non-significant).

See also Table S2 and Figure S4.

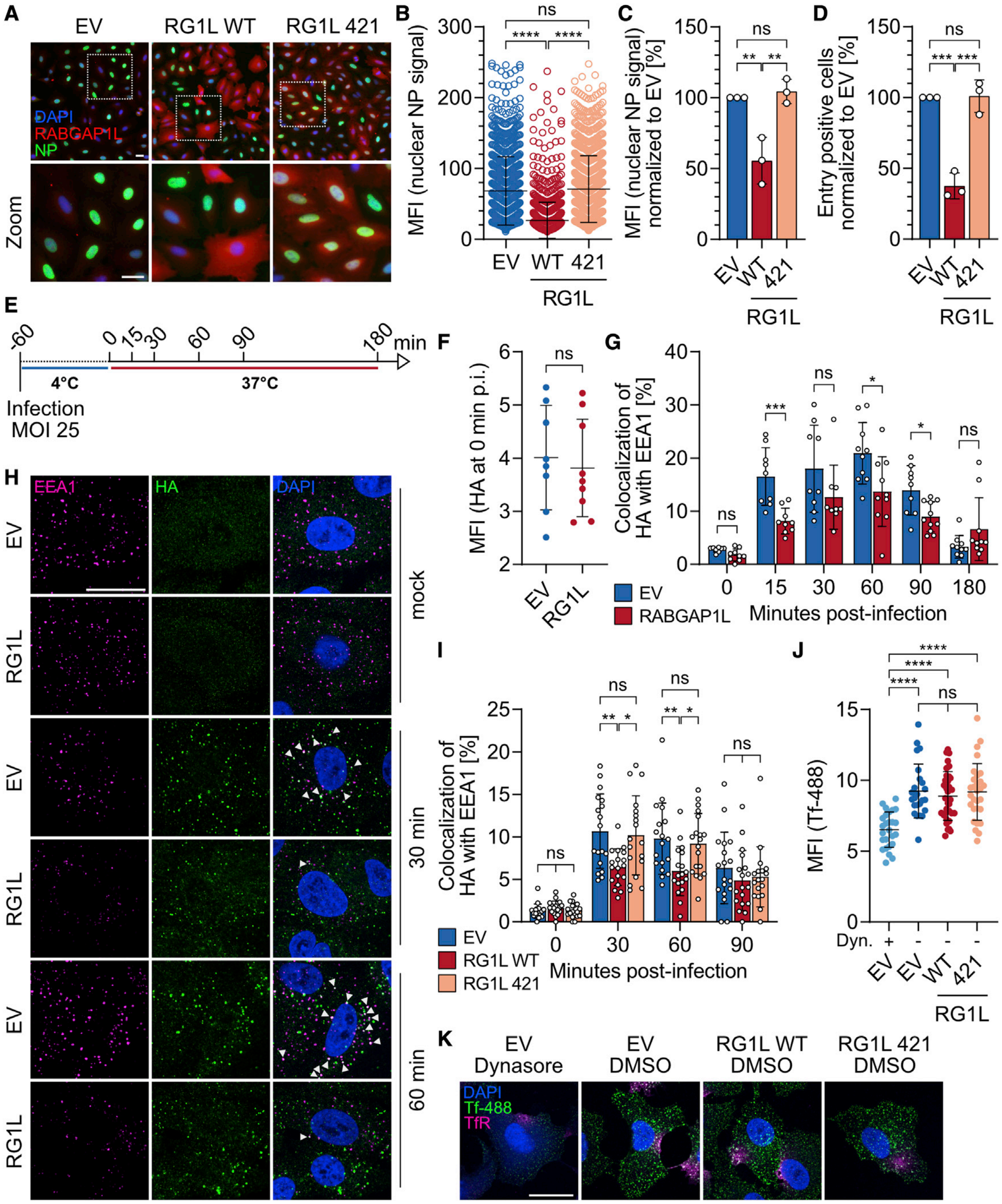

Figure 6. RABGAP1L expression impacts host endosomal function and IAV uptake

(A–C) A549 cells stably expressing RABGAP1L WT, the 421-truncation mutant, or EV were infected with WSN/33 (MOI 5 PFU/cell) for 1 h on ice. Three hours after incubation at 37°C, cells were fixed and stained with antibodies against RABGAP1L (red) and NP (green) (A). Nuclei were stained with DAPI (blue). Scale bar represents 25 μm.

(B and C) Green mean fluorescent intensities (MFIs) of nuclear NP signals were quantified from fluorescent-microscopy images from (A) using ImageJ software. Individual cells are represented by single dots (B). Mean values of data from three biologically independent experiments in (B), normalized to EV, are shown in (C).

(D) MDCK cells, expressing the constructs described in (A), were infected for 4 h at 37°C with WSN/33-pseudotyped β-lactamase-matrix protein (BlaM1) fusion protein VLPs prior to quantification of entry-positive cells via flow cytometry. Data represent means, with error bars showing SDs, from three biologically independent experiments. Individual data points are shown.

(E) Experimental setup for immunofluorescence-based confocal microscopy to track early stages during IAV entry. Following infection with WSN/33 (MOI 25 PFU/cell or mock) for 1 h at 4°C, cells were fixed at the indicated timepoints.

(legend continued on next page)

T-V5-RG1L or T-V5-GFP-NES expressing A549 cells were stimulated with 1,000 U/mL IFNα2 (or mock) for 16 h prior to addition of biotin for 15 min (Figure 5E). After cell lysis and streptavidin-based affinity purification, differentially biotinylated proteins were analyzed by mass spectrometry and identified by SaintExpress. Across three independent biological replicates, 13 putative interaction partners specific to RABGAP1L were identified, many of which included proteins with reported activities in several aspects of endosomal and autophagosomal function (Figure 5F; Table S2). For example, the endosomal sorting complex required for transport II (ESCRT-II) subunit SNF8, also known as VPS22 or EAP30, is involved in endosomal sorting of ubiquitinated membrane proteins (Raiborg and Stenmark, 2009), while the zinc-finger protein ZFP91 is an important regulator of the non-canonical nuclear factor κB (NF-κB) pathway (Jin et al., 2010) and plays a role in autophagosome maturation (Wang et al., 2021). In line with the RAB GTPase-activating function of RABGAP1L, it was notable that the single RAB GTPase protein RAB27B was identified as a putative interactor of RABGAP1L. Our data indicate that PL is a powerful method to identify RABGAP1L interactors and confirm that RABGAP1L likely functions in pathways associated with vesicle biology.

Antivirally active RABGAP1L engages with the VPS33A component of membrane tethering complexes

We focused our attention on the interaction of RABGAP1L with VPS33A, a component of two hexameric tethering complexes, the class C core vacuole/endosome tethering (CORVET) complex and the homotypic fusion and protein sorting (HOPS) complex (Balderhaar and Ungermann, 2013; Chou et al., 2016), which are key regulators of the mammalian endosomal machinery (van der Beek et al., 2019). CORVET is essential for the homotypic fusion of RAB5-positive early endosomes, whereas HOPS mediates heterotypic fusion events between RAB7-positive late endosomes or autophagosomes with lysosomes, a function shown to depend on the VPS33A core subunit (van der Beek et al., 2019; Wartosch et al., 2015). These complexes were of interest to us given the involvement of endosomal trafficking in the IAV entry process (Sempere Borau and Stertz, 2021). To validate the RABGAP1L-VPS33A interaction, we re-performed PL and affinity purification experiments and confirmed the specific proximal association of the two proteins by western blot (Figure 5G). Notably, this interaction appeared to be specific to a ∼75 kDa form of VPS33A that may represent an unknown post-translationally modified form of the protein (Figure 5G). Furthermore, it was striking that this form of VPS33A was not biotinylated when the antivirally inactive RABGAP1L mutants (KK_{mut}, impacting endosomal trafficking; RQ_{mut}, impacting TBC-domain function) were used (Figure 5G), indicating that the interaction is likely to be important for the antiviral function of RABGAP1L. However, while siRNAs targeting *VPS33A* led to a small increase in WSN/33-*Renilla* IAV replication in the presence of IFNα2, depletion of VPS33A alone was insufficient to counteract the IFN-dependent antiviral effect of RABGAP1L overexpression (Figures S4A and S4B). Similar results were noted in parallel assays with other identified endosomal RABGAP1L interactors, including RAB27B and SNF8 (Figures S4A and S4B). This may suggest that multiple factors redundantly support RABGAP1L function or that this particular assay setup is not sufficiently sensitive to uncover co-operation. Nevertheless, these data highlight a previously undescribed interaction between VPS33A and antivirally active RABGAP1L that might implicate changes to endosomal functions during RABGAP1L-mediated virus restriction.

RABGAP1L expression impacts host endosomal structure and IAV uptake

We note that IAV, VSV, and HCoV-229E (viruses restricted by RABGAP1L) primarily enter the tested cells by endocytosis (Kawase et al., 2009; Mercer et al., 2010), while SARS-CoV-2, SeV, and NDV (all resistant to the action of RABGAP1L) mainly enter the tested cells by fusing at the plasma membrane or, under some limited circumstances, in endosomes (Chang and Dutch, 2012; Koch et al., 2021). Given this, together with the proteomic indications that RABGAP1L appears to engage with the endosomal machinery, we further investigated the specific action of RABGAP1L at individual stages of the IAV replication cycle. First, we monitored the expression of nuclear viral nucleoprotein (NP) signal in an immunofluorescence-based assay 3 h post-infection of cells with IAV as a marker of early viral replication events. In A549 cells transduced with an empty vector, the nuclear NP signal was typically strong at this time point but was markedly reduced in infected cells that overexpressed full-length RABGAP1L (Figures 6A–6C). Notably, overexpression of the

---

(F) A549 cells stably expressing RABGAP1L (RG1L) or EV were subjected to the experimental setup described in (E). The MFI of HA signals (green) at 0 min p.i. were quantified from confocal-microscopy images shown in Figure S6A using ImageJ. Individual cells are represented by single dots.

(G) Quantification of co-localizations between EEA1 and HA from confocal images shown in (H) and Figure S6A using Imaris. Individual cells are represented by single dots.

(H) Immunofluorescence analysis of RABGAP1L or EV-expressing A549 cells treated as described in (E). Cells were stained for early endosomes (EEA1, magenta), viral proteins (HA, green), and nuclei (DAPI, blue). Scale bar represents 25 μm. White arrows indicate co-localizations between EEA1 and HA. Representative images of at least nine analyzed cells per time point from at least two biologically independent experiments.

(I) Quantification of co-localizations between EEA1 and HA from confocal images shown in Figure S6B. Individual cells are represented by single dots.

(J and K) Cells described in (A) were serum starved for 2 h prior to treatment with Dynasore (Dyn.; 100 μm) or DMSO for 1 h at 37°C. Cells were then incubated with Alexa-Fluor-488-conjugated transferrin (Tf-488) for 1 h at 4°C followed by a 10-min incubation at 37°C prior to fixation.

(J) MFI quantification of Tf-488 signals from confocal-microscopy images shown in (K) using ImageJ software. Individual cells are represented by single dots.

(K) Cells were stained with anti-transferrin receptor (TfR) antibody (magenta) and DAPI (blue) prior to analysis by confocal microscopy. Scale bar represents 25 μm. Representative images of at least 25 analyzed cells from two biologically independent experiments.

Statistical significance was determined using unpaired nonparametric t test (B, F, G, and J), unpaired one-way ANOVA (C and D), or ordinary two-way ANOVA (I) (*$p < 0.05$, **$p < 0.002$, ***$p < 0.001$, ****$p < 0.0001$; ns, non-significant).

See also Figures S5–S7.

antivirally inactive RABGAP1L-421 truncation mutant did not appreciably affect the viral NP signal, which looked similar to that of empty-vector-transduced cells (Figures 6A–6C). Since the monitored NP signal could originate from both incoming and newly synthesized NPs, we next investigated the effects of RABGAP1L expression on viral polymerase activity using a standard IAV mini-replicon system. RABGAP1L overexpression, unlike the known IAV inhibitor murine Mx1, had no effect on IAV mini-replicon activity, indicating that the action of RABGAP1L on viral infection must precede viral gene transcription in the nucleus (Figures S5A and S5B). Indeed, overexpression of full-length RABGAP1L, but not the antivirally inactive RABGAP1L-421 truncation mutant, was able to inhibit a stage of viral infection preceding or including fusion of the viral membrane with cellular membranes, as assessed by a flow-cytometry-based virus-like particle (BlaM1-VLP) assay that measures infection immediately after fusion (Figure 6D) (Tscherne et al., 2010). However, using immunofluorescence-based confocal microscopy to track both IAV proteins and various markers of the endo-lysosomal pathway during virus entry (Figure 6E), we observed that IAV attachment to cells was not affected by RABGAP1L overexpression (Figures 6F and S6A), suggesting that RABGAP1L mediates its effects subsequent to viral uptake but at or before fusion. Furthermore, we noted that puncta positive for early endosome antigen 1 (EEA1; a specific marker for early endosomes) appeared to be less detectable and smaller in size during infection of cells expressing RABGAP1L, and the co-localization between EEA1 and IAV HA was generally reduced (Figures 6G, 6H, and S6A). The size of HA-positive puncta also appeared to be smaller in RABGAP1L-overexpressing cells. These effects were not generally observed in cells expressing the antivirally inactive RABGAP1L-421 truncation mutant (Figures 6I and S6B). Notably, western blot analysis revealed that overexpression of RABGAP1L did not impact total levels of EEA1 during IAV infection (Figure S6C), suggesting a restructuring of EEA1-positive puncta with full-length RABGAP1L rather than EEA1 degradation. Similar to the EEA1 staining, signal intensities for lysobisphosphatidic acid (LBPA; a marker of late endosomes and endo-lysosomes [Mercer and Helenius, 2009]) were harder to detect in RABGAP1L-expressing cells during IAV infection, suggesting a broad effect of RABGAP1L on endosomal function (Figure S7A). Indeed, this effect was less pronounced for lysosomal-associated membrane protein 1 (LAMP1; a marker of lysosomes and late endosomes) (Figure S7B), implying specificity to the intracellular vesicles impacted by RABGAP1L. However, not all endocytic cargoes appear to be affected by RABGAP1L overexpression, as we did not detect an impact of RABGAP1L on uptake of transferrin (Figures 6J and 6K). Altogether, these data suggest that RABGAP1L restricts IAV, and potentially other endocytic viruses, at an early stage of the viral replication cycle by disturbing an infection-specific endosomal function and limiting viral-fusion-mediated entry.

DISCUSSION

Herein, we performed an RNAi screen targeting 100 putative ISGs with previously undescribed contributions to IFN-mediated IAV restriction and identified eight human genes that limit early stages of the IAV replication cycle. Among these, we further characterized the RABGAP1L protein, finding that RABGAP1L overexpression strongly potentiates the antiviral action of IFNα2 against IAV and can also inhibit viruses such as VSV and HCoV-229E. Notably, these viruses primarily enter cells via endocytosis, and indeed, RABGAP1L overexpression disrupted normal endosomal function during IAV entry, leading to the prevention of IAV particle fusion with cellular membranes. In particular, our immunofluorescence-based studies of IAV entry in RABGAP1L-overexpressing cells revealed smaller clusters of HA and reduced co-localization with early endosomes. Our proteomic analyses of RABGAP1L interactors provided a possible mechanistic basis for these observations and have contributed to our working hypothesis on the antiviral action of RABGAP1L (see Figure 7). In our currently favored model, the interaction of RABGAP1L with the core VPS33A component of the cellular CORVET and HOPS complexes leads to the increased fusion of early endosomes with lysosomes, potentially promoting the lysosomal degradation of incoming viral particles that are undergoing endocytosis. Support for our model, and the importance of the RABGAP1L:VPS33A interaction, comes from our observation that antivirally inactive mutants of RABGAP1L fail to interact with VPS33A. However, studies from others have shown that high levels of RABGAP1L induce the GTPase activity of RAB5A (and possibly RAB22A), a key protein localizing to early endosomes, and lead to loss of detectable EEA1 staining in immunofluorescence assays (Itoh et al., 2006), similar to our findings. Interestingly, recruitment of both AnkB and RABGAP1L promoted the dissociation of RAB22A from β1-integrin-containing endosomes, initiating their transition from RAB5-positive early endosomes to RAB5-negative recycling endosomes (Qu et al., 2016), and a mutant RABGAP1L lacking the AnkB-binding site failed to restrict IAV. Thus, it is possible that other non-degradative mechanisms to limit IAV entry can occur. Nevertheless, it is known that the VPS33A-containing HOPS complex mediates fusion events between late endosomes/autophagosomes and lysosomes (van der Beek et al., 2019; Wartosch et al., 2015). Furthermore, a recent study also observed co-localization between RABGAP1L and the known HOPS-binding protein RAB7 at the site of endo-lysosomes (Golden et al., 2021). Together with our work, these findings implicate RABGAP1L-mediated disruption of an endosomal function as a mechanism for restricting IAV entry. Strikingly, we found that SARS-CoV-2 and two paramyxoviruses appeared to be resistant to the inhibitory effects of overexpressed RABGAP1L. Given that these viruses enter cells primarily at the plasma membrane (Chang and Dutch, 2012; Koch et al., 2021), these observations lend weight to the idea that RABGAP1L targets viruses that exclusively use the endocytic route for entry. Furthermore, a non-viral endocytic cargo, transferrin, was not impacted by RABGAP1L overexpression, suggesting that the effect of RABGAP1L may actually be specific to certain endocytic entry routes triggered by infection.

Surprisingly, despite *RABGAP1L* being previously noted as an ISG in primary human hepatocytes (He et al., 2010) and therefore included in our putative ISG siRNA library, we were unable to confirm this observation in the range of transformed cell lines and primary cells used here. Nevertheless, an independent study

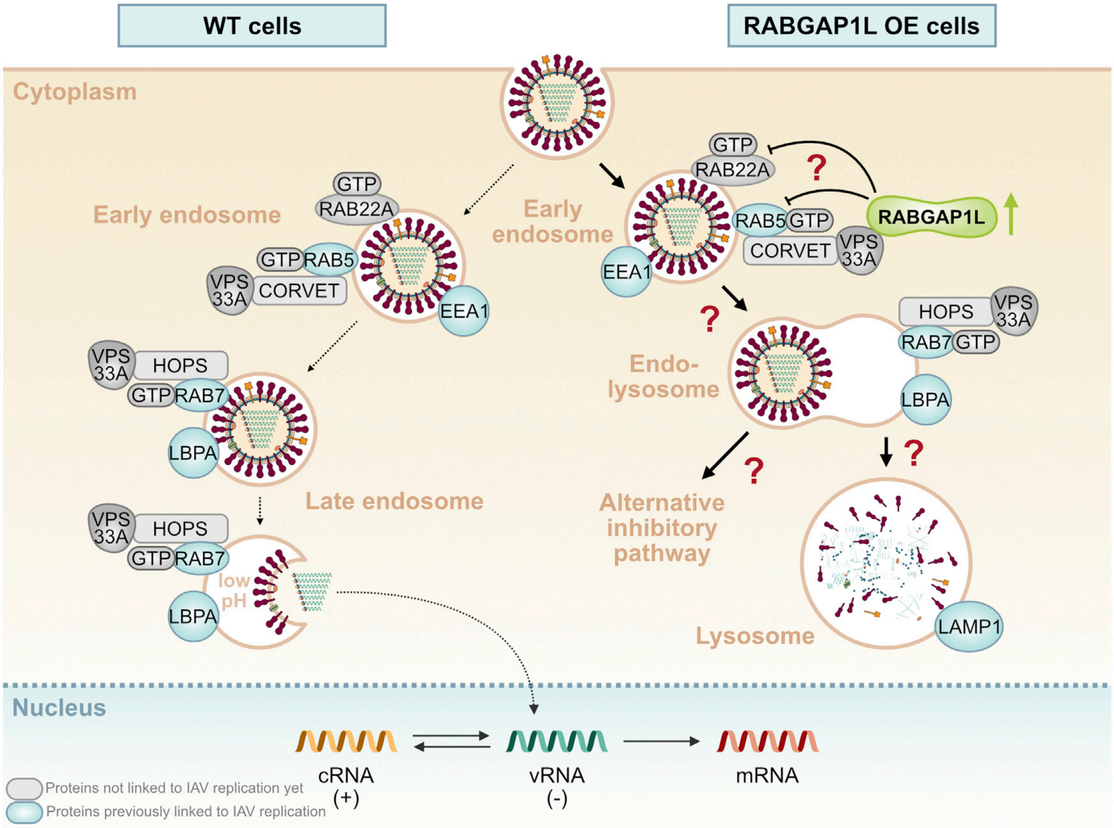

Figure 7. Hypothetical model of viral restriction by RABGAP1L

In WT cells, IAVs enter via endocytosis. Early endosomes mature into late endosomes where the low pH induces HA-mediated fusion between the viral and endosomal membranes, leading to the release of the viral genome into the cytoplasm and its transport to the nucleus for replication and transcription. Active GTP-bound RAB22A and RAB5, as well as EEA1, are known to localize to early endosomes and have been found to interact with each other (Kauppi et al., 2002; Zhu et al., 2009). The CORVET complex, including its core subunit VPS33A, associates with RAB5 on early endosomes (Spang, 2016; Wartosch et al., 2015). Maturation to late endosomes is marked by a RAB5 to RAB7 switch and dissociation of EEA1 and RAB22A (Rink et al., 2005; Zhu et al., 2009). LBPA is a marker found on late endo and endo-lysosomes (Gruenberg, 2020). The HOPS complex, including its core subunit VPS33A, is known to associate with RAB7 on late endosomes and to mediate fusion with lysosomes (Balderhaar and Ungermann, 2013; Poteryaev et al., 2010). In cells overexpressing RABGAP1L, RABGAP1L may associate with VPS33A at IAV-containing early endosomes and potentially promotes a more rapid maturation from early to late endosomes by deactivation of RAB22A and/or RAB5 (Itoh et al., 2006). Dissociation of the two RABs and EEA1 from early endosomes drives the maturation of endosomes, which fuse with lysosomes to form endo-lysosomes (Bright et al., 2016; Luzio et al., 2014). Association of RABGAP1L with VPS33A of the HOPS complex might enhance this process. Maturation to lysosomes could initiate the degradation of the endocytosed viral particle by lysosomal proteases, ultimately limiting infection. LAMP1 is found mainly on lysosomes. Proteins marked in blue are known to colocalize with IAV particles (Liu et al., 2014; Sieczkarski and Whittaker, 2003).

also identified *RABGAP1L* as an ISG (albeit weakly induced) in primary human fibroblasts (Shaw et al., 2017), implying that, under certain circumstances or in certain cell types, its expression can be boosted by IFN and aid in virus-entry restriction. Nevertheless, it was clear from many of our experiments that the antiviral activity of (overexpressed) RABGAP1L was higher in the presence of exogenously applied IFN. We thus hypothesize that RABGAP1L might act in parallel to additional ISG products to limit endocytic virus entry, for example, the known inhibitors IFITM3 or NCOA7 (Brass et al., 2009; Doyle et al., 2018), and together, these factors slow endocytic virus entry. However, we cannot rule out the intriguing possibility that RABGAP1L directly engages with some additional ISG products to support its proposed function in driving endo-lysosomal trafficking. In this regard, we note that RAB27B, which we identified as a putative RABGAP1L interactor by PL, has also been described as an ISG product (Shaw et al., 2017). The deactivation and dissociation of RAB GTPases from bound vesicles induced by RABGAP proteins is a critical step during endosomal maturation and trafficking (Frasa et al., 2012). RAB27B has been proposed to control different steps of the exosome-secretion pathway (Ostrowski et al., 2010). Since exosomes are formed from late endosomes or multivesicular bodies (Hessvik and Llorente, 2018), deactivation of RAB27B by RABGAP1L might limit exosomal secretion and instead favor the fusion of virus-containing endocytic vesicles with lysosomes. Thus, in summary, it is striking that IFN appears to induce a number of proteins involved in either regulating endosomal function or inhibiting key virus-entry features, such as virus-host membrane fusion. This underscores that inhibiting virus entry is a critically important pillar of host antiviral defenses. Furthermore, together with the recent identification of another TBC-domain-containing protein as an inhibitor of IAV replication (TBC1D5) (Martin-Sancho et al., 2021), our study supports an emerging picture that multiple RAB-specific GTPase-activating proteins potentiate the host IFN response by modulating different aspects of host vesicle biology.

Limitations of the study

While our siRNA screen uncovered eight human genes that inhibit the early stages of IAV replication in an IFN-dependent manner, the experimental approach used did result in some constraints. Firstly, the number of target genes that could be included in our siRNA library was limited, and target inclusion was not based on target expression in the cells used but rather on the selected functional bias. Secondly, the single-cycle IAV reporter system limits the identification of factors that impact infection at later stages of the virus replication cycle. Thirdly, our use of a WT human IAV strain does not take into account the likelihood that some IAVs may have evolved antagonistic functions to selected antiviral human genes, such that antiviral activity may be more apparent with specific IAV mutants or non-human strains. Lastly, our targeting of individual genes prevents the discovery of co-operation or redundancy between factors. There will be many more antiviral human genes identified and characterized with strategies that overcome these limitations.

STAR★METHODS

Detailed methods are provided in the online version of this paper and include the following:

- KEY RESOURCES TABLE
- RESOURCE AVAILABILITY
  - ○ Lead contact
  - ○ Materials availability
  - ○ Data and code availability
- EXPERIMENTAL MODEL AND SUBJECT DETAILS
  - ○ Cells
  - ○ Viruses
- METHOD DETAILS
  - ○ Interferon treatments
  - ○ Infection assays
  - ○ Cell viability assays
  - ○ Plasmid cloning and stable cell-lines
  - ○ RNA interference
  - ○ SDS-PAGE and western blotting
  - ○ Immunofluorescence
  - ○ Transferrin uptake assay
  - ○ RT-qPCR analysis
  - ○ Mini-replicon and mini-genome assay
  - ○ Flow cytometry-based BlaM1-VLP assay
  - ○ Proximity labeling
- QUANTIFICATION AND STATISTICAL ANALYSIS
  - ○ Colocalization quantification using Imaris
  - ○ MFI quantification using ImageJ
  - ○ Statistical analysis

SUPPLEMENTAL INFORMATION

Supplemental information can be found online at https://doi.org/10.1016/j.celrep.2022.110549.

ACKNOWLEDGMENTS

We thank Volker Thiel, Jovan Pavlovic, and Adolfo García-Sastre for providing essential reagents and Samira Schiefer, Marie Pohl, Davide Eletto, and Eva Moritz (University of Zurich) for helpful advice or technical support. Proteomic analyses were performed with support from the Functional Genomics Center Zurich. Flow cytometry was performed with support from the Cytometry Facility, University of Zurich. The research leading to these results received funding from the Swiss National Science Foundation (grants 31003A_182464 to B.G.H. and 31003A_176170 to S.S.) and the University of Zurich (Forschungskredit grant FK-20-030 to S.F.). The funders had no role in study design, data collection, data interpretation, or the decision to submit the work for publication.

AUTHOR CONTRIBUTIONS

Conceptualization, S.F., S.S., and B.G.H.; methodology, S.F. and E.E.S.; investigation: S.F., E.E.S., I.B., U.K., and A.L.; writing – original draft, S.F. and B.G.H.; writing – review & editing, S.F., E.E.S., I.B., U.K., A.L., S.S., and B.G.H.; visualization, S.F.; supervision & project administration, B.G.H.; funding acquisition, S.F., S.S., and B.G.H.

DECLARATION OF INTERESTS

The authors declare no competing interests.

Received: October 6, 2021
Revised: January 31, 2022
Accepted: March 1, 2022
Published: March 22, 2022

REFERENCES

Balderhaar, H.J., and Ungermann, C. (2013). CORVET and HOPS tethering complexes - coordinators of endosome and lysosome fusion. J. Cell Sci. *126*, 1307–1316. https://doi.org/10.1242/jcs.107805.

Borold, J., Eletto, D., Busnadiego, I., Mair, N.K., Moritz, E., Schiefer, S., Schmidt, N., Petric, P.P., Wong, W.W., Schwemmle, M., and Hale, B.G. (2021). BRD9 is a druggable component of interferon-stimulated gene expression and antiviral activity. EMBO Rep. *22*, e52823. https://doi.org/10.15252/embr.202152823.

Brass, A.L., Huang, I.C., Benita, Y., John, S.P., Krishnan, M.N., Feeley, E.M., Ryan, B.J., Weyer, J.L., van der Weyden, L., Fikrig, E., et al. (2009). The IFITM proteins mediate cellular resistance to influenza A H1N1 virus, West Nile virus, and dengue virus. Cell *139*, 1243–1254. https://doi.org/10.1016/j.cell.2009.12.017.

Braun, E., Hotter, D., Koepke, L., Zech, F., Gross, R., Sparrer, K.M.J., Muller, J.A., Pfaller, C.K., Heusinger, E., Wombacher, R., et al. (2019). Guanylate-binding proteins 2 and 5 exert broad antiviral activity by inhibiting furin-mediated processing of viral envelope proteins. Cell Rep. *27*, 2092–2104.e2010. https://doi.org/10.1016/j.celrep.2019.04.063.

Bright, N.A., Davis, L.J., and Luzio, J.P. (2016). Endolysosomes are the principal intracellular sites of acid hydrolase activity. Curr. Biol. *26*, 2233–2245. https://doi.org/10.1016/j.cub.2016.06.046.

Busnadiego, I., Fernbach, S., Pohl, M.O., Karakus, U., Huber, M., Trkola, A., Stertz, S., and Hale, B.G. (2020). Antiviral activity of type I, II, and III interferons counterbalances ACE2 inducibility and restricts SARS-CoV-2. mBio *11*. https://doi.org/10.1128/mBio.01928-20.

Busse, D.C., Habgood-Coote, D., Clare, S., Brandt, C., Bassano, I., Kaforou, M., Herberg, J., Levin, M., Eleouet, J.F., Kellam, P., and Tregoning, J.S. (2020). Interferon-induced protein 44 and interferon-induced protein 44-like restrict replication of respiratory syncytial virus. J. Virol. *94*. https://doi.org/10.1128/JVI.00297-20.

Chang, A., and Dutch, R.E. (2012). Paramyxovirus fusion and entry: multiple paths to a common end. Viruses *4*, 613–636. https://doi.org/10.3390/v4040613.

Cho, K.F., Branon, T.C., Udeshi, N.D., Myers, S.A., Carr, S.A., and Ting, A.Y. (2020). Proximity labeling in mammalian cells with TurboID and split-TurboID. Nat. Protoc. *15*, 3971–3999. https://doi.org/10.1038/s41596-020-0399-0.

Chou, H.T., Dukovski, D., Chambers, M.G., Reinisch, K.M., and Walz, T. (2016). CATCHR, HOPS and CORVET tethering complexes share a similar architecture. Nat. Struct. Mol. Biol. *23*, 761–763. https://doi.org/10.1038/nsmb.3264.

Desai, T.M., Marin, M., Chin, C.R., Savidis, G., Brass, A.L., and Melikyan, G.B. (2014). IFITM3 restricts influenza A virus entry by blocking the formation of fusion pores following virus-endosome hemifusion. PLoS Pathog. *10*, e1004048. https://doi.org/10.1371/journal.ppat.1004048.

Domingues, P., Golebiowski, F., Tatham, M.H., Lopes, A.M., Taggart, A., Hay, R.T., and Hale, B.G. (2015). Global reprogramming of host SUMOylation during influenza virus infection. Cell Rep. *13*, 1467–1480. https://doi.org/10.1016/j.celrep.2015.10.001.

Doyle, T., Moncorge, O., Bonaventure, B., Pollpeter, D., Lussignol, M., Tauziet, M., Apolonia, L., Catanese, M.T., Goujon, C., and Malim, M.H. (2018). The interferon-inducible isoform of NCOA7 inhibits endosome-mediated viral entry. Nat. Microbiol. *3*, 1369–1376. https://doi.org/10.1038/s41564-018-0273-9.

Frasa, M.A., Koessmeier, K.T., Ahmadian, M.R., and Braga, V.M. (2012). Illuminating the functional and structural repertoire of human TBC/RABGAPs. Nat. Rev. Mol. Cell Biol *13*, 67–73. https://doi.org/10.1038/nrm3267.

Golden, E., Rashwan, R., Woodward, E.A., Sgro, A., Wang, E., Sorolla, A., Waryah, C., Tie, W.J., Cuyas, E., Ratajska, M., et al. (2021). The oncogene AAMDC links PI3K-AKT-mTOR signaling with metabolic reprograming in estrogen receptor-positive breast cancer. Nat. Commun. *12*, 1920. https://doi.org/10.1038/s41467-021-22101-7.

Gruenberg, J. (2020). Life in the lumen: the multivesicular endosome. Traffic *21*, 76–93. https://doi.org/10.1111/tra.12715.

He, X.S., Nanda, S., Ji, X., Calderon-Rodriguez, G.M., Greenberg, H.B., and Liang, T.J. (2010). Differential transcriptional responses to interferon-alpha and interferon-gamma in primary human hepatocytes. J. Interferon Cytokine Res. *30*, 311–320. https://doi.org/10.1089/jir.2009.0082.

Hessvik, N.P., and Llorente, A. (2018). Current knowledge on exosome biogenesis and release. Cell Mol. Life Sci. *75*, 193–208. https://doi.org/10.1007/s00018-017-2595-9.

Itoh, T., Satoh, M., Kanno, E., and Fukuda, M. (2006). Screening for target Rabs of TBC (Tre-2/Bub2/Cdc16) domain-containing proteins based on their Rab-binding activity. Genes Cells *11*, 1023–1037. https://doi.org/10.1111/j.1365-2443.2006.00997.x.

Iwasaki, A., and Pillai, P.S. (2014). Innate immunity to influenza virus infection. Nat. Rev. Immunol. *14*, 315–328. https://doi.org/10.1038/nri3665.

Jin, X., Jin, H.R., Jung, H.S., Lee, S.J., Lee, J.H., and Lee, J.J. (2010). An atypical E3 ligase zinc finger protein 91 stabilizes and activates NF-kappaB-inducing kinase via Lys63-linked ubiquitination. J. Biol. Chem. *285*, 30539–30547. https://doi.org/10.1074/jbc.M110.129551.

Kane, M., Zang, T.M., Rihn, S.J., Zhang, F., Kueck, T., Alim, M., Schoggins, J., Rice, C.M., Wilson, S.J., and Bieniasz, P.D. (2016). Identification of interferon-stimulated genes with antiretroviral activity. Cell Host Microbe *20*, 392–405. https://doi.org/10.1016/j.chom.2016.08.005.

Karakus, U., Thamamongood, T., Ciminski, K., Ran, W., Gunther, S.C., Pohl, M.O., Eletto, D., Jeney, C., Hoffmann, D., Reiche, S., et al. (2019). MHC class II proteins mediate cross-species entry of bat influenza viruses. Nature *567*, 109–112. https://doi.org/10.1038/s41586-019-0955-3.

Kauppi, M., Simonsen, A., Bremnes, B., Vieira, A., Callaghan, J., Stenmark, H., and Olkkonen, V.M. (2002). The small GTPase Rab22 interacts with EEA1 and controls endosomal membrane trafficking. J. Cell Sci. *115*, 899–911.

Kawase, M., Shirato, K., Matsuyama, S., and Taguchi, F. (2009). Protease-mediated entry via the endosome of human coronavirus 229E. J. Virol. *83*, 712–721. https://doi.org/10.1128/JVI.01933-08.

Koch, J., Uckeley, Z.M., Doldan, P., Stanifer, M., Boulant, S., and Lozach, P.Y. (2021). TMPRSS2 expression dictates the entry route used by SARS-CoV-2 to infect host cells. EMBO J. *40*, e107821. https://doi.org/10.15252/embj.2021107821.

Krammer, F., Smith, G.J.D., Fouchier, R.A.M., Peiris, M., Kedzierska, K., Doherty, P.C., Palese, P., Shaw, M.L., Treanor, J., Webster, R.G., and Garcia-Sastre, A. (2018). Influenza. Nat. Rev. Dis. Primers *4*, 3. https://doi.org/10.1038/s41572-018-0002-y.

Kuroda, M., Halfmann, P.J., Hill-Batorski, L., Ozawa, M., Lopes, T.J.S., Neumann, G., Schoggins, J.W., Rice, C.M., and Kawaoka, Y. (2020). Identification of interferon-stimulated genes that attenuate Ebola virus infection. Nat. Commun. *11*, 2953. https://doi.org/10.1038/s41467-020-16768-7.

Li, J., Ding, S.C., Cho, H., Chung, B.C., Gale, M., Jr., Chanda, S.K., and Diamond, M.S. (2013). A short hairpin RNA screen of interferon-stimulated genes identifies a novel negative regulator of the cellular antiviral response. mBio. *4*, e00385, 00313. https://doi.org/10.1128/mBio.00385-13.

Liu, S.L., Wu, Q.M., Zhang, L.J., Wang, Z.G., Sun, E.Z., Zhang, Z.L., and Pang, D.W. (2014). Three-dimensional tracking of Rab5- and Rab7-associated infection process of influenza virus. Small *10*, 4746–4753. https://doi.org/10.1002/smll.201400944.

Liu, S.Y., Sanchez, D.J., Aliyari, R., Lu, S., and Cheng, G. (2012). Systematic identification of type I and type II interferon-induced antiviral factors. Proc. Natl. Acad. Sci. U S A *109*, 4239–4244. https://doi.org/10.1073/pnas.1114981109.

Long, J.S., Mistry, B., Haslam, S.M., and Barclay, W.S. (2019). Host and viral determinants of influenza A virus species specificity. Nat. Rev. Microbiol. *17*, 67–81. https://doi.org/10.1038/s41579-018-0115-z.

Luzio, J.P., Hackmann, Y., Dieckmann, N.M., and Griffiths, G.M. (2014). The biogenesis of lysosomes and lysosome-related organelles. Cold Spring Harb. Perspect. Biol. *6*, a016840. https://doi.org/10.1101/cshperspect.a016840.

Mar, K.B., Rinkenberger, N.R., Boys, I.N., Eitson, J.L., McDougal, M.B., Richardson, R.B., and Schoggins, J.W. (2018). LY6E mediates an evolutionarily conserved enhancement of virus infection by targeting a late entry step. Nat. Commun. *9*, 3603. https://doi.org/10.1038/s41467-018-06000-y.

Martin-Sancho, L., Tripathi, S., Rodriguez-Frandsen, A., Pache, L., Sanchez-Aparicio, M., McGregor, M.J., Haas, K.M., Swaney, D.L., Nguyen, T.T., Mamede, J.I., et al. (2021). Restriction factor compendium for influenza A virus reveals a mechanism for evasion of autophagy. Nat. Microbiol. *6*, 1319–1333. https://doi.org/10.1038/s41564-021-00964-2.

Menachery, V.D., Eisfeld, A.J., Schafer, A., Josset, L., Sims, A.C., Proll, S., Fan, S., Li, C., Neumann, G., Tilton, S.C., et al. (2014). Pathogenic influenza viruses and coronaviruses utilize similar and contrasting approaches to control interferon-stimulated gene responses. mBio *5*, e01174, 01114. https://doi.org/10.1128/mBio.01174-14.

Mercer, J., and Helenius, A. (2009). Virus entry by macropinocytosis. Nat. Cell Biol. *11*, 510–520. https://doi.org/10.1038/ncb0509-510.

Mercer, J., Schelhaas, M., and Helenius, A. (2010). Virus entry by endocytosis. Annu. Rev. Biochem. *79*, 803–833. https://doi.org/10.1146/annurev-biochem-060208-104626.

Ostrowski, M., Carmo, N.B., Krumeich, S., Fanget, I., Raposo, G., Savina, A., Moita, C.F., Schauer, K., Hume, A.N., Freitas, R.P., et al. (2010). Rab27a and Rab27b control different steps of the exosome secretion pathway. Nat. Cell Biol. *12*, 19–30. https://doi.org/10.1038/ncb2000.

Pan, X., Eathiraj, S., Munson, M., and Lambright, D.G. (2006). TBC-domain GAPs for Rab GTPases accelerate GTP hydrolysis by a dual-finger mechanism. Nature *442*, 303–306. https://doi.org/10.1038/nature04847.

Perez-Riverol, Y., Csordas, A., Bai, J., Bernal-Llinares, M., Hewapathirana, S., Kundu, D.J., Inuganti, A., Griss, J., Mayer, G., Eisenacher, M., et al. (2019). The PRIDE database and related tools and resources in 2019: improving support for quantification data. Nucleic Acids Res. *47*, D442–D450. https://doi.org/10.1093/nar/gky1106.

Pfaender, S., Mar, K.B., Michailidis, E., Kratzel, A., Boys, I.N., V'Kovski, P., Fan, W., Kelly, J.N., Hirt, D., Ebert, N., et al. (2020). LY6E impairs coronavirus fusion and confers immune control of viral disease. Nat. Microbiol. *5*, 1330–1339. https://doi.org/10.1038/s41564-020-0769-y.

Pohl, M.O., Busnadiego, I., Kufner, V., Glas, I., Karakus, U., Schmutz, S., Zaheri, M., Abela, I., Trkola, A., Huber, M., et al. (2021). SARS-CoV-2 variants reveal features critical for replication in primary human cells. PLoS Biol. *19*, e3001006. https://doi.org/10.1371/journal.pbio.3001006.

Poteryaev, D., Datta, S., Ackema, K., Zerial, M., and Spang, A. (2010). Identification of the switch in early-to-late endosome transition. Cell *141*, 497–508. https://doi.org/10.1016/j.cell.2010.03.011.

Qu, F., Lorenzo, D.N., King, S.J., Brooks, R., Bear, J.E., and Bennett, V. (2016). Ankyrin-B is a PI3P effector that promotes polarized alpha5beta1-integrin recycling via recruiting RabGAP1L to early endosomes. Elife *5*. https://doi.org/10.7554/eLife.20417.

Raiborg, C., and Stenmark, H. (2009). The ESCRT machinery in endosomal sorting of ubiquitylated membrane proteins. Nature *458*, 445–452. https://doi.org/10.1038/nature07961.

Rink, J., Ghigo, E., Kalaidzidis, Y., and Zerial, M. (2005). Rab conversion as a mechanism of progression from early to late endosomes. Cell *122*, 735–749. https://doi.org/10.1016/j.cell.2005.06.043.

Sanchez-Aparicio, M.T., Garcin, D., Rice, C.M., Kolakofsky, D., Garcia-Sastre, A., and Baum, A. (2017). Loss of Sendai virus C protein leads to accumulation of RIG-I immunostimulatory defective interfering RNA. J. Gen. Virol. *98*, 1282–1293. https://doi.org/10.1099/jgv.0.000815.

Schmidt, N., Domingues, P., Golebiowski, F., Patzina, C., Tatham, M.H., Hay, R.T., and Hale, B.G. (2019). An influenza virus-triggered SUMO switch orchestrates co-opted endogenous retroviruses to stimulate host antiviral immunity. Proc. Natl. Acad. Sci. U S A *116*, 17399–17408. https://doi.org/10.1073/pnas.1907031116.

Schoggins, J.W. (2019). Interferon-stimulated genes: what do they all do? Annu. Rev. Virol. *6*, 567–584. https://doi.org/10.1146/annurev-virology-092818-015756.

Schoggins, J.W., MacDuff, D.A., Imanaka, N., Gainey, M.D., Shrestha, B., Eitson, J.L., Mar, K.B., Richardson, R.B., Ratushny, A.V., Litvak, V., et al. (2014). Pan-viral specificity of IFN-induced genes reveals new roles for cGAS in innate immunity. Nature *505*, 691–695. https://doi.org/10.1038/nature12862.

Schoggins, J.W., Wilson, S.J., Panis, M., Murphy, M.Y., Jones, C.T., Bieniasz, P., and Rice, C.M. (2011). A diverse range of gene products are effectors of the type I interferon antiviral response. Nature *472*, 481–485. https://doi.org/10.1038/nature09907.

Sempere Borau, M., and Stertz, S. (2021). Entry of influenza A virus into host cells - recent progress and remaining challenges. Curr. Opin. Virol. *48*, 23–29. https://doi.org/10.1016/j.coviro.2021.03.001.

Shaw, A.E., Hughes, J., Gu, Q., Behdenna, A., Singer, J.B., Dennis, T., Orton, R.J., Varela, M., Gifford, R.J., Wilson, S.J., and Palmarini, M. (2017). Fundamental properties of the mammalian innate immune system revealed by multispecies comparison of type I interferon responses. PLoS Biol. *15*, e2004086. https://doi.org/10.1371/journal.pbio.2004086.

Sieczkarski, S.B., and Whittaker, G.R. (2003). Differential requirements of Rab5 and Rab7 for endocytosis of influenza and other enveloped viruses. Traffic *4*, 333–343. https://doi.org/10.1034/j.1600-0854.2003.00090.x.

Spang, A. (2016). Membrane tethering complexes in the endosomal system. Front. Cell Dev. Biol. *4*, 35. https://doi.org/10.3389/fcell.2016.00035.

Spieler, E.E., Moritz, E., Stertz, S., and Hale, B.G. (2020). Application of a biologically contained reporter system to study gain-of-function H5N1 influenza A viruses with pandemic potential. mSphere *5*. https://doi.org/10.1128/mSphere.00423-20.

Steiner, F., and Pavlovic, J. (2020). Subcellular localization of MxB determines its antiviral potential against influenza A virus. J. Virol. *94*. https://doi.org/10.1128/JVI.00125-20.

Tran, V., Ledwith, M.P., Thamamongood, T., Higgins, C.A., Tripathi, S., Chang, M.W., Benner, C., Garcia-Sastre, A., Schwemmle, M., Boon, A.C.M., et al. (2020). Influenza virus repurposes the antiviral protein IFIT2 to promote translation of viral mRNAs. Nat. Microbiol. *5*, 1490–1503. https://doi.org/10.1038/s41564-020-0778-x.

Tripathi, S., Pohl, M.O., Zhou, Y., Rodriguez-Frandsen, A., Wang, G., Stein, D.A., Moulton, H.M., DeJesus, P., Che, J., Mulder, L.C., et al. (2015). Meta- and orthogonal integration of influenza "OMICs" data defines a role for UBR4 in virus budding. Cell Host Microbe *18*, 723–735. https://doi.org/10.1016/j.chom.2015.11.002.

Tscherne, D.M., Manicassamy, B., and Garcia-Sastre, A. (2010). An enzymatic virus-like particle assay for sensitive detection of virus entry. J. Virol. Methods *163*, 336–343. https://doi.org/10.1016/j.jviromet.2009.10.020.

Turkington, H.L., Juozapaitis, M., Kerry, P.S., Aydillo, T., Ayllon, J., Garcia-Sastre, A., Schwemmle, M., and Hale, B.G. (2015). Novel bat influenza virus NS1 proteins bind double-stranded RNA and antagonize host innate immunity. J. Virol. *89*, 10696–10701. https://doi.org/10.1128/JVI.01430-15.

van den Worm, S.H., Eriksson, K.K., Zevenhoven, J.C., Weber, F., Zust, R., Kuri, T., Dijkman, R., Chang, G., Siddell, S.G., Snijder, E.J., et al. (2012). Reverse genetics of SARS-related coronavirus using vaccinia virus-based recombination. PLoS One *7*, e32857. https://doi.org/10.1371/journal.pone.0032857.

van der Beek, J., Jonker, C., van der Welle, R., Liv, N., and Klumperman, J. (2019). CORVET, CHEVI and HOPS - multisubunit tethers of the endo-lysosomal system in health and disease. J. Cell Sci. *132*. https://doi.org/10.1242/jcs.189134.

Wang, A., Ding, L., Wu, Z., Ding, R., Teng, X.L., Wang, F., Hu, Z., Chen, L., Yu, X., and Zou, Q. (2021). ZFP91 is required for the maintenance of regulatory T cell homeostasis and function. J. Exp. Med. *218*. https://doi.org/10.1084/jem.20201217.

Wartosch, L., Gunesdogan, U., Graham, S.C., and Luzio, J.P. (2015). Recruitment of VPS33A to HOPS by VPS16 is required for lysosome fusion with endosomes and autophagosomes. Traffic *16*, 727–742. https://doi.org/10.1111/tra.12283.

Wilson, S.J., Schoggins, J.W., Zang, T., Kutluay, S.B., Jouvenet, N., Alim, M.A., Bitzegeio, J., Rice, C.M., and Bieniasz, P.D. (2012). Inhibition of HIV-1 particle assembly by 2′,3′-cyclic-nucleotide 3′-phosphodiesterase. Cell Host Microbe *12*, 585–597. https://doi.org/10.1016/j.chom.2012.08.012.

Zhao, X., Zheng, S., Chen, D., Zheng, M., Li, X., Li, G., Lin, H., Chang, J., Zeng, H., and Guo, J.T. (2020). LY6E restricts entry of human coronaviruses, including currently pandemic SARS-CoV-2. J. Virol. *94*, e00562, 00520. https://doi.org/10.1128/JVI.00562-20.

Zhu, H., Liang, Z., and Li, G. (2009). Rabex-5 is a Rab22 effector and mediates a Rab22-Rab5 signaling cascade in endocytosis. Mol. Biol. Cell *20*, 4720–4729. https://doi.org/10.1091/mbc.E09-06-0453.

STAR★METHODS

KEY RESOURCES TABLE

REAGENT or RESOURCE	SOURCE	IDENTIFIER
Antibodies		
Actin rabbit polyclonal	Sigma-Aldrich	Cat#A2103, RRID: AB_476694
β-actin mouse monoclonal (C4)	Santa Cruz	Cat#sc-47778, RRID: AB_2714189
RABGAP1L rabbit polyclonal	Proteintech	Cat#13894-1-AP, RRID: AB_10638308
MxA mouse monoclonal (ab143)	Jovan Pavlovic	Steiner and Pavlovic, 2020
STAT1 mouse monoclonal	Santa Cruz	Cat#sc-417, RRID: AB_675902
Phospho-STAT1 (Tyr701) (D4A7) rabbit monoclonal	Cell Signaling	Cat#7649, RRID: AB_10950970
IFI44 rabbit polyclonal	Atlas Antibodies	Cat#HPA043858, RRID: AB_2678702
FLAG M2 mouse monoclonal	Sigma-Aldrich	Cat#F1804, RRID: AB_262044
IAV-PB1 rabbit polyclonal	GeneTex	Cat#GTX125923, RRID: AB_2753122
IAV-PB2 rabbit	Domingues et al., 2015	N/A
IAV-PA rabbit polyclonal	GeneTex	Cat#GTX118991, RRID: AB_10619959
IAV-NP (HB-65) mouse monoclonal	ATCC	Cat#H16-L10-4R5, RRID: CVCL_4524
V5 mouse monoclonal	Bio-Rad	Cat#MCA1360, RRID: AB_322378
VPS33A rabbit polyclonal	Proteintech	Cat#16896-1-AP, RRID: AB_2214916)
RAB27B rabbit polyclonal	Proteintech	Cat#13412-1-AP, RRID: AB_2176732
EAP30 (C-11) (SNF8) mouse monoclonal	Santa Cruz	Cat#sc-390747
A/WSN/33 HA1 rabbit polyclonal	Sino Biological	Cat#11692-T54
EEA1 mouse monoclonal	BD Bioscience	Cat#610457, RRID: AB_397830
EEA1 rabbit polyclonal	Cell Signaling	Cat#2411, RRID: AB_2096814
LBPA mouse	Echelon	Cat#Z-PLBPA, RRID: AB_11129226
LAMP1 rabbit polyclonal	abcam	Cat#ab24170, RRID: AB_775978
Transferrin receptor mouse monoclonal	Thermo Fisher Scientific	Cat#13–6800, RRID: AB_2533029
IRDye 800CW goat anti-mouse IgG	Li-Cor	Cat#926–32210, RRID: AB_621842
IRDye 800CW goat anti-rabbit IgG	Li-Cor	Cat#926–32211, RRID: AB_621843
IRDye 680CW goat anti-mouse IgG	Li-Cor	Cat#926–68070, RRID: AB_10956588
IRDye 680CW goat anti-rabbit IgG	Li-Cor	Cat#926–68071, RRID: AB_10956166
Donkey anti-mouse IgG Alexa Fluor 488	Thermo Fisher Scientific	Cat#A-21202, RRID: AB_141607
Donkey anti-rabbit IgG Alexa Fluor 488	Thermo Fisher Scientific	Cat#A-21206, RRID: AB_2535792
Donkey anti-mouse IgG Alexa Fluor 555	Thermo Fisher Scientific	Cat#A-31570, RRID: AB_2536180
Donkey anti-rabbit IgG Alexa Fluor 555	Thermo Fisher Scientific	Cat#A32794, RRID: AB_2762834
Donkey anti-mouse IgG Alexa Fluor 647	Thermo Fisher Scientific	Cat#A32787, RRID: AB_2762830
Donkey anti-rabbit IgG Alexa Fluor 647	Thermo Fisher Scientific	Cat#A32795, RRID: AB_2762835
DAPI	Sigma-Aldrich	Cat#10236276001
Bacterial and virus strains		
A/WSN/33 (H1N1)	This study	N/A
A/WSN/33-*Renilla* (H1N1)	Spieler et al., 2020	N/A
A/Netherlands/602/09-*Renilla* (pdmH1N1)	Spieler et al., 2020	N/A
A/Vietnam/1203/04-*Renilla* (H5N1)	Spieler et al., 2020	N/A
HCoV-229E-*Renilla*	Volker Thiel	van den Worm et al., 2012
VSV-GFP	Adolfo Garcia-Sastre	N/A
SeV-GFP	Adolfo Garcia-Sastre	Sanchez-Aparicio et al., 2017

(*Continued on next page*)

Continued

REAGENT or RESOURCE	SOURCE	IDENTIFIER
NDV-GFP	Adolfo Garcia-Sastre	N/A
SARS-CoV-2/human/Switzerland/IMV5/2020	Busnadiego et al., 2020	N/A
Chemicals, peptides, and recombinant proteins		
Recombinant Human IFN-alpha 2 Protein	Novusbio	Cat#NBP2-34971
Recombinant Human IFN Beta 1b	Pbl assay science	Cat#11420-1
Recombinant Human IFN-gamma Protein	Novusbio	Cat#NBP2-34992
Recombinant Human IL-29/IFN-lambda 1 Protein	Novusbio	Cat#NBP2-34996
Dimethyl sulfoxide (DMSO)	Sigma-Aldrich	Cat#D8418
Transferrin From Human Serum, Alexa Fluor^{TM} 488 Conjugate	Thermo Fisher Scientific	Cat#T13342
Dynasore	Merck	Cat#D7693
Lipofectamine RNAiMAX	Invitrogen	Cat#13778150
OptiMEM	Life Technologies	Cat#31985062
FuGENE® HD transfection reagent	Promega	Cat#E2311
EnduRen^{TM} Live Cell Substrate	Promega	Cat#E6482
TPCK-trypsin	Sigma-Aldrich	Cat#4370285
16% paraformaldehyde	Lucerna Chem	Cat#EMS15710
Triton X-100	Promega	Cat#H5142
ProLong Gold Antifade Mountant	Life Technologies	Cat#P36930
Airway Epithelial Cell Growth Medium	PromoCell	Cat#C-21260
Airway Epithelial Cell Growth Medium SupplementPack	PromoCell	Cat#C-39160
Y-27632 dihydrochloride	Selleck Chemicals	Cat#1254
FluoroBrite^{TM} DMEM	Life Technologies	Cat#A1896701
Ammonium chloride	Sigma-Aldrich	Cat#254134
Saponin	Sigma-Aldrich	Cat#47036
Bovine serum albumin (BSA)	Sigma-Aldrich	Cat#A7906
DEAE-dextran hydrochloride	Sigma-Aldrich	Cat#D9885
CCF2-AM	Thermo Fisher Scientific	Cat#K1032
Biotin	Sigma-Aldrich	Cat#B4501-1G
cOmplete^{TM}, Mini Protease Inhibitor Cocktail	Roche	Cat#11836153001
PhosSTOP^{TM}	Roche	Cat#4906837001
Pierce^{TM} Streptavidin Magnetic Beads	Thermo Fisher Scientific	Cat#88817
Tris hydrochloride (Tris-HCl)	Sigma-Aldrich	Cat#10812846001
Potassium chloride (KCl)	Sigma-Aldrich	Cat#60130
Sodium carbonate (Na_2CO_3)	Sigma-Aldrich	Cat#31432
Ammonium bicarbonate (NH_4HCO_3)	Sigma-Aldrich	Cat#A6141
Paraformaldehyde	Electron Microscopy Sciences	Cat#19208
Critical commercial assays		
SuperScript III reverse transcriptase	Thermo Fisher Scientific	Cat#18080044
CellTiter-Glo Luminescent Cell Viability Assay	Promega	Cat#G7570
QuikChange II XL Site-Directed Mutagenesis Kit	Agilent Technologies	Cat#200522
In-Fusion HD Cloning Plus Kit	Takara	Cat#638910
ReliaPrep^{TM} RNA Miniprep Systems	Promega	Cat#Z6012

(*Continued on next page*)

Continued

REAGENT or RESOURCE	SOURCE	IDENTIFIER
Fast EvaGreen qPCR Master Mix Kit	Biotium	Cat#31003-1
Dual-Glo Luciferase Assay System	Promega	Cat#E2980
LIVE/DEAD^{TM} Fixable Near-IR Dead Cell Stain Kit	Thermo Fisher Scientific	Cat#L10119
Deposited data		
Investigating the interactome of TurboID-tagged RABGAP1L in the presence or absence of IFNa2 by proximity labeling proteomics	ProteomeXchange	PXD029960
Experimental models: Cell lines		
Human: lung carcinoma cell line A549	ATCC	CCL-185
Human: lung adenocarcinoma cell line Calu-3	ATCC	HTB-55
Human: embryonic kidney cell line HEK293T	ATCC	CRL-11268
Human: HeLa cells	ATCC	CCL-2
Human: Huh-7 cells	Volker Thiel	van den Worm et al., 2012
Human: U87-MG cells	ATCC	HTB-14
MRC-5-hTert	Turkington et al., 2015	N/A
Human primary bronchial epithelial cell (BEpC) cultures from a 73-year-old female	PromoCell	Cat#C-12640
Canis familiaris: Madin-Darby Canine Kidney cell line MDCK	ATCC	CCL-34
Cercopithecus aethiops: Vero-CCL81 cells	ATCC	CCL-81
Cercopithecus aethiops: Vero-E6 cells	ATCC	CRL-1586
Oligonucleotides		
Oligonucleotides (see Tables S1 and S3)	This study	N/A
Recombinant DNA		
pLVX-RABGAP1L-A-IRES-Puro	This study	N/A
pLVX-RABGAP1L-G-IRES-Puro	This study	N/A
pLVX-RABGAP1L-H-IRES-Puro	This study	N/A
pLVX-RABGAP1L-I-IRES-Puro	This study	N/A
p3xFLAG-RABGAP1L-A	This study	N/A
p3xFLAG-RABGAP1L-421	This study	N/A
p3xFLAG-mCherry	This study	N/A
p3xFLAG-Mx1	This study	N/A
pLVX-TurboID-V5-GFP-NES-IRES-Puro	Borold et al., 2021	N/A
pLVX-TurboID-V5-RABGAP1L-A-IRES-Puro	This study	N/A
pLVX-RABGAP1L-delTBC-IRES-Puro	This study	N/A
pLVX-RABGAP1L-421-IRES-Puro	This study	N/A
pLVX-RABGAP1L-340-IRES-Puro	This study	N/A
pLVX-RABGAP1L-257-IRES-Puro	This study	N/A
pLVX-RABGAP1L-R584A-IRES-Puro	This study	N/A
pLVX-RABGAP1L-Q621A-IRES-Puro	This study	N/A
pLVX-RABGAP1L-R584A-Q621A-IRES-Puro	This study	N/A
pLVX-RABGAP1L-KK784EE-IRES-Puro	This study	N/A
pCAGGS-WSN/33-PB1	Domingues et al., 2015	N/A
pCAGGS-WSN/33-PB2	Domingues et al., 2015	N/A
pCAGGS-WSN/33-PA	Domingues et al., 2015	N/A

(*Continued on next page*)

Continued

REAGENT or RESOURCE	SOURCE	IDENTIFIER
pCAGGS-WSN/33-NP	Domingues et al., 2015	N/A
pPol-I-FFluc	Domingues et al., 2015	N/A
pRL-SV40	Domingues et al., 2015	N/A
pPol-FF-luc-358	Domingues et al., 2015	N/A
Software and algorithms		
IncuCyte ZOOM software (v.2018A)	Sartorius	https://www.essenbioscience.com/en/resources/incucyte-zoom-resources-support/software-modules-incucyte-zoom/
GraphPad Prism (v.9.1.2)	GraphPad Software	https://www.graphpad.com/scientific-software/prism/
LAS X	Leica	https://www.leica-microsystems.com/de/produkte/mikroskop-software/p/leica-las-x-ls/
Image Studio Light (v.5.2))	LI-COR Biosciences	https://www.licor.com/bio/image-studio-lite/
FlowJo (v.10)	BD	https://www.flowjo.com/solutions/flowjo
Imaris (v. 9.7.2)	Oxford Instruments	https://imaris.oxinst.com/
ImageJ	National Institutes of Health, Bethesda, USA	https://imagej.nih.gov/ij/
7300 System SDS Software Core Application (v.1.4)	Applied Biosystems	N/A
SaintExpress algorithm	CRAPome	https://reprint-apms.org/?q=analysis_front_apms
Other		
7300 Real-Time PCR System	Applied Biosystems	N/A
EnVision Multimode Microplate Reader	PerkinElmer	Cat#2105-0010
Odissey Fc imaging system	LI-COR Biosciences	N/A
LEICA SP8 (or SP5) upright confocal laser scanning microscope	Leica	N/A
FACSVerse System	BD	N/A
Leica DMIL LED upright microscope and Leica DFC7000 T camera	Leica	N/A

RESOURCE AVAILABILITY

Lead contact

Further information and requests for resources and reagents should be directed to the lead contact, Benjamin G. Hale (hale.ben@virology.uzh.ch).

Materials availability

All unique reagents generated in this study are available from the lead contact without restriction.

Data and code availability

Mass spectrometry data have been deposited to the ProteomeXchange Consortium via the PRIDE (Perez-Riverol et al., 2019) partner repository with the dataset identifier PXD029960. The data are publicly available as of the date of publication.

This paper does not report original code.

Any additional information required to reanalyze the data reported in this paper is available from the lead contact upon request.

EXPERIMENTAL MODEL AND SUBJECT DETAILS

Cells

A549, MDCK, Calu-3, 293T, HeLa, Huh-7, U87-MG, Vero-CCL81 and Vero-E6 cells were cultured at 37°C and 5% CO_2 in Dulbecco's Modified Eagle's Medium (DMEM, Life Technologies), supplemented with 10% (v/v) fetal calf serum (FCS), 100 units/mL of penicillin and 100 μg/mL of streptomycin (Life Technologies). Exceptionally, 20% (v/v) FCS was used for Calu-3 cells. MRC-5-hTert cells were cultured in Minimum Essential Medium Eagle (MEM, Sigma-Aldrich) supplemented with 10% (v/v) FCS, 100 units/mL of penicillin, 100 μg/mL of streptomycin, 2 mM L-Glutamine and 1% (v/v) Non-Essential Amino Acids (Life Technologies) (Turkington et al., 2015). MRC-5-hTert cells expressing the WSN/33 IAV HA protein were previously described (Spieler et al., 2020). Primary human BEpCs from a 73-year-old female donor were purchased from PromoCell, Germany (catalog no. C-12640). Cells were grown in airway epithelium basal growth medium (PromoCell, catalog no. C-21260) supplemented with an airway growth medium supplement pack (PromoCell, catalog no. C-39160) and 10 μM Y-27632 (Selleck Chemicals, USA). BEpCs were differentiated and validated as described (Busnadiego et al., 2020; Pohl et al., 2021).

Viruses

A/WSN/33 IAV was propagated and titrated in MDCK cells. Propagation and use of biologically-contained *Renilla* luciferase-encoding IAVs based on A/WSN/33 (WSN/33), A/Netherlands/602/09 (pdmH1N1) and A/Vietnam/1203/04 (H5N1) has been described previously (Spieler et al., 2020). HCoV-229E-*Renilla* was kindly provided by Volker Thiel, University of Bern, Switzerland (van den Worm et al., 2012). VSV-GFP, NDV-GFP and SeV-GFP were kind gifts from Adolfo García-Sastre, Icahn School of Medicine, New York, USA (Sanchez-Aparicio et al., 2017). Propagation and titration of SARS-CoV-2 has been previously described (Busnadiego et al., 2020; Pohl et al., 2021).

METHOD DETAILS

Interferon treatments

Recombinant IFNα2 (catalog no. NBP2-34971; Novusbio), IFNβ1b (catalog no. 11420-1, pbl assay science), IFNγ (catalog no. NBP2-34992; Novusbio) and IFNλ1 (catalog no. NBP2-34996, Novusbio) were used at the indicated concentrations and were diluted in DMEM supplemented with 10% (v/v) FCS, 100 units/mL of penicillin and 100 μg/mL of streptomycin. For BEpCs, IFNs were added to the apical compartment in phosphate-buffered saline (PBS).

Infection assays

For infections with *Renilla*-encoding viruses, 1 × 10^4 cells were seeded into 96-well plates and 32 h later stimulated (or mock) with IFNα2 at the indicated concentrations. 16 h later, viruses were diluted in PBSi (supplemented with 0.3% BSA, 100 units/mL of penicillin, 100 μg/mL of streptomycin, and 1 mM Ca^{2+}/Mg^{2+}) and cells were infected at the indicated multiplicity of infection (MOI) for 1 h at 37°C. After infection, cells were washed with PBS and then overlaid with post-infection (p.i.) DMEM (supplemented with 0.1% FBS, 100 units/mL penicillin, 100 μg/mL streptomycin, 0.3% BSA, and 20 mM HEPES) in the presence of 1 μg/mL TPCK-trypsin (Sigma-Aldrich) and 6μM EnduRen™ Live Cell Substrate (Promega). Luminescence was measured at the indicated time points using the EnVision Multilabel Reader (Perkin Elmer). Area under the curve (AUC) values were determined from the obtained relative light units (RLUs) using GraphPad Prism software.

For infections with wild-type WSN/33 or SARS-CoV-2, 1.5 × 10^5 cells/well were seeded in 12-well plates (or 1 × 10^5 for 24-well plates) and stimulated with the indicated concentrations of IFNα2 for 16 h. Virus inoculum was prepared in PBSi and cells were infected at the indicated MOI. After 1 h incubation at 37°C, cells were washed with PBS and then overlaid with p.i. DMEM supplemented with 1 μg/mL TPCK-trypsin. Supernatant was collected at the indicated time points and stored at −80°C prior to titration by plaque assay on MDCK cells (for WSN/33) or Vero-E6 cells (for SARS-CoV-2) cells.

For VSV-GFP, NDV-GFP and SeV-GFP, 2 × 10^4 cells/well were seeded into a 96-well plate one day prior to stimulation (or mock treatment) with IFNα2 at the indicated concentration for 4 h or 16 h. Cells were washed with PBS and then incubated with virus at the indicated MOI diluted in Fluorobrite DMEM (Life Technologies) supplemented with 2% (v/v) FCS, 100 units/mL penicillin, 100 μg/mL streptomycin, and 2 mM L-glutamine. GFP expression was monitored for up to 72 h using IncuCyte ZOOM Live-Cell Imaging System (Sartorius). Total Green Integrated Intensity (Green Calibrated Unit × μm^2/image) values were used to calculate the area under the curve (AUC).

Cell viability assays

Cell viability was measured at the indicated times after siRNA transfection using the CellTiter-Glo Luminescent Cell Viability Assay (Promega, #G7570) according to the manufacturer's protocol.

Plasmid cloning and stable cell-lines

Codon-optimized *RABGAP1L* isoforms A (NM_014857), G (NM_001366446) and I (NM_001366448) were synthesized using GeneArt Gene Synthesis (Life Technologies) and cloned into pLVX-IRES-Puro (Clontech) and p3xFLAG-CMV-7.1 (Sigma-Aldrich) plasmids using EcoRI and XbaI restriction sites. Isoform H (NM_001366447) was generated from p3xFLAG-RABGAP1L-A using In-Fusion cloning (Takara), following the manufacturer's protocol. Truncated versions of RABGAP1L were generated by PCR, and point mutations were created using site-directed mutagenesis (QuikChange II XL; Agilent Technologies) with p3xFLAG-RABGAP1L-A as the starting template before sub-cloning into pLVX-IRES-Puro. pLVX-IRES-Puro based GFP or TurboID-V5 constructs were generated as described (Borold et al., 2021). Inserts for all constructs were confirmed by Sanger sequencing. All oligo sequences are listed in (Table S3). To generate cell-lines stably expressing the appropriate constructs, cells were transduced with lentiviral particles produced by co-transfecting 293T cells with the respective pLVX-IRES-Puro derived construct, pMD2.G and pCMVdR8.91 (Schmidt et al., 2019) in the presence of polybrene (8 μg/mL, Sigma-Aldrich). 48 h later, stably-transduced cells were selected for puromycin resistance (Thermo Fisher Scientific; 1 μg/mL for A549 and Calu-3, 2 μg/mL for MDCK, and 3 μg/mL for Vero-CCL81 cells).

RNA interference

Cells were reverse transfected with siRNAs (final concentration: 30 nM) diluted in OptiMEM (Life Technologies) using Lipofectamine RNAiMAX (Life Technologies) according to the manufacturer's protocol. 32 h post-transfection, cells were stimulated (or mock-treated) with 1000 U/mL IFNα2 for 16 h, prior to infection with IAV WSN/33-*Renilla* (MOI 1 or 5 PFU/cell). All siRNA sequences including additional screen information are listed in Table S1. The genes selected for targeting with the siRNA library were derived from previous datasets of putative ISGs identified in various cell-lines (He et al., 2010; Li et al., 2013; Menachery et al., 2014; Schoggins et al., 2011), and were cross-referenced with genome-wide screening meta-analyses to identify promising IAV restriction factors (Tripathi et al., 2015), prior to function-based cherry-picking that largely excluded well-characterized ISGs.

SDS-PAGE and western blotting

Cell samples were lysed in 2× urea disruption buffer (6 M urea, 2 M β-mercaptoethanol, and 4% SDS) and sonicated to shear nucleic acids. Following treatment at 95°C for 5 min, proteins were separated by SDS-polyacrylamide gel electrophoresis (SDS-PAGE) on NuPAGE 4–12% Bis-Tris gradient gels (Life Technologies), followed by transfer to nitrocellulose membranes (GE Healthcare Life Sciences). Proteins were detected by western blotting using the following primary antibodies: actin (rabbit, catalog no. A2103; Sigma-Aldrich), β-actin (mouse, catalog no.sc-47778; Santa Cruz), RABGAP1L (rabbit, catalog no. 13894-1-AP; proteintech), MxA (mouse ab143, kindly provided by Jovan Pavlovic, University of Zurich) (Steiner and Pavlovic, 2020), STAT1 (mouse, catalog no. sc-417; Santa Cruz), pSTAT1-Y701 (rabbit, catalog no. 7649S; Cell Signaling), IFI44 (rabbit, catalog no. HPA043858; Atlas Antibodies), FLAG M2 (mouse, catalog no. F1804; Sigma-Aldrich), PB1 (rabbit, catalog no. GTX125923; Genetex), PB2 (rabbit, inhouse), PA (rabbit, catalog no. GTX118991; Genetex), NP (mouse HB65, catalog no. H16-L10-4R5, ATCC), V5 (mouse, catalog no. MCA1360; Bio-Rad), VPS33A (rabbit, catalog no. 16896-1-AP, proteintech), RAB27B (rabbit, catalog no. 13412-1-AP, proteintech), SNF8 (mouse, catalog no. sc-390747, Santa Cruz), A/WSN/33 HA1 (rabbit, catalog no. 11692-T54; Sino Biological) and EEA1 (rabbit, catalog no. 2411, Cell Signaling). The following secondary antibodies were used: IRDye 800CW goat anti-mouse IgG (catalog no. 926–32210; Li-Cor), IRDye 800CW goat anti-rabbit IgG (catalog no. 926–32211; Li-Cor), IRDye 680CW goat anti-mouse IgG (catalog no. 926–68070; Li-Cor) and IRDye 680CW goat anti-rabbit IgG (catalog no. 926–68071; Li-Cor). A LI-COR Odyssey Fc scanner was used for detection.

Immunofluorescence

Approximately 7.5 × 10^4 cells were seeded onto glass coverslips in a 24-well plate for 24 h. For uninfected cells, cells were fixed for 15 min with 3.5% paraformaldehyde (PFA) and permeabilized for 5 min using 0.5% Triton X-100 in PBS. After blocking with 2% FBS in PBS for 30 min, staining with primary and secondary antibodies (listed below) was performed in PBS with 2% FBS for 1 h each. For infection-based assays, WSN was diluted in PBSi to reach the indicated MOI. The cells were stored for 15 min on ice before they were washed once with PBS. The inoculum was added on ice for 1 h to synchronize the infection. The inoculum was removed and replaced by p.i. DMEM, and the cells were incubated for the indicated times at 37°C. Cells were then fixed for 15 min with 3.5% PFA and permeabilized for at least 1 h using confocal buffer (PBS supplemented with 50 mM ammonium chloride (catalog no. 254134; Sigma-Aldrich), 0.1% saponin (catalog no. 47036; Sigma-Aldrich) and 2% BSA (catalog no. A7906; Sigma-Aldrich)). Primary and secondary antibodies were diluted in confocal buffer and incubated with samples for at least 1 h before coverslips were mounted using ProLong Gold Antifade Mountant (catalog no. P36930; Thermo Fisher Scientific). Images were acquired on an SP5 or SP8 confocal microscope (Leica) or on a DMIL LED fluorescent microscope (Leica). The following primary antibodies were used: RABGAP1L (rabbit, catalog no. 13894-1-AP; proteintech), NP (mouse HB65, catalog no. H16-L10-4R5, ATCC), V5 (mouse, catalog no. MCA1360; Bio-Rad), A/WSN/33 HA1 (rabbit, catalog no. 11692-T54; Sino Biological), EEA1 (mouse, catalog no. 610457; BD Bioscience), LAMP1 (rabbit, catalog no. ab24170; abcam), and LBPA (mouse, catalog no. Z-PLBPA; Echelon). Secondary antibodies were: donkey anti-mouse IgG Alexa Fluor 488 (catalog no. A21202; Thermo Fisher Scientific), donkey anti-rabbit IgG Alexa Fluor 488 (catalog no. A21206; Thermo Fisher Scientific), donkey anti-mouse IgG Alexa Fluor 555 (catalog no. A31570; Thermo Fisher Scientific), donkey anti-rabbit IgG Alexa Fluor 555 (catalog no. A32794; Thermo Fisher Scientific), donkey anti-mouse IgG Alexa Fluor 647 (catalog no. A32787; Thermo Fisher Scientific), and donkey anti-rabbit IgG Alexa Fluor 647 (catalog no. A32795; Thermo Fisher Scientific). DAPI (catalog no. 10236276001, Sigma-Aldrich) was used to stain nuclei.

Transferrin uptake assay

Approximately 5 × 10^4 cells were seeded onto glass coverslips in a 24-well plate for 24 h. Cells were washed once with PBS and pre-incubated with serum-free DMEM for 2 h. Dynasore (100 μM or DMSO) was added to the cells in serum-free DMEM for 1 h at 37°C. The cells were then incubated with 10 μg/mL of Alexa 488-conjugated transferrin (Thermo Fisher Scientific, catalog no. T13342) in serum-free medium and in the presence of Dynasore (or DMSO) for 1 h at 4°C. Cells were then shifted to 37°C for 10 min to allow uptake of transferrin, washed twice with PBS and fixed in 3.5% PFA. Cells were stained with a primary antibody for the transferrin receptor (catalog no. 13–6800, Thermo Fisher Scientific) and DAPI (catalog no. 10236276001, Sigma-Aldrich), prior to secondary staining and imaging as detailed above.

RT-qPCR analysis

RNA extraction from cells was performed using the Reliaprep RNA cell kit (Promega) according to the manufacturer's instructions. cDNA was synthesized from 1 μg of total RNA using Superscript III reverse transcriptase (ThermoFisher) and an Oligo(dT)$_{15}$ primer (Promega). RT-qPCR was performed on a 7300 Real-Time PCR system (Applied Biosystems) using a Fast EvaGreen qPCR Master Mix Kit (Biotium). Primers used are listed in Table S3. The Delta-delta-cycle threshold (ΔΔCt) was determined relative to untreated control samples. Gene expression was normalized to GAPDH.

Mini-replicon and mini-genome assay

The mini-replicon assay was performed as previously described (Domingues et al., 2015). Briefly, 293T cells were co-transfected with expression plasmids (pCAGGS) encoding WSN PB1, PB2, PA and NP, a negative-sense RNA polymerase I (Pol-I) driven Firefly luciferase reporter construct (pPol-I-FFluc), a constitutively transcribed *Renilla* luciferase plasmid (pRL-SV40), and increasing concentrations of 3xFLAG-tagged plasmids expressing mCherry, mouse Mx1, RABGAP1L WT or the 421 mutant. 24 h post-transfection, cells were lysed and luciferase activity was measured using the Dual-Glo Luciferase Assay System (Promega). Firefly luciferase values were normalized to *Renilla* luciferase activity; all samples were normalized to a no PB2 control. For the mini-genome assay, 293T cells were transiently co-transfected with a negative-sense viral-like Firefly luciferase reporter construct (pPol-FF-luc-358), a constitutively transcribed *Renilla* luciferase plasmid (pRL-SV40) and increasing concentrations of 3xFLAG-tagged plasmids expressing mCherry, Mx1, RABGAP1L WT or the 421 mutant. Cells were infected with WSN/33 (MOI 0.01 PFU/cell or mock) for 24 h before cells were lysed and the luciferase activity was measured. Firefly luciferase values were normalized to *Renilla* luciferase activity; all samples were normalized to mock.

Flow cytometry-based BlaM1-VLP assay

Generation of VLPs expressing a BlaM1 fusion protein consisting of a β-lactamase (Bla) and the matrix protein (M1) from WSN have been described previously (Karakus et al., 2019; Tscherne et al., 2010). For infection, MDCK cells were washed with PBS followed by incubation with 200 μL of BlaM1 VLPs supplemented with 0.1 μg/mL DEAE–dextran hydrochloride and 2% FCS for 4 h at 37°C. Cells were collected by trypsinization and loaded with the fluorogenic β-lactamase substrate CCF2-AM (catalog no. K1032; Thermo Fisher Scientific). Sample analysis was performed on a FACSVerse System (BD); dead cells were excluded using the LIVE/DEAD^{TM} Fixable Near-IR Dead Cell Stain Kit (catalog no. L10119; Thermo Fisher Scientific). Entry-positive cells were quantified by gating on events with cleaved CCF2-AM using FlowJo v.10 software.

Proximity labeling

2×10^6 A549 cells stably expressing the indicated TurboID-V5 constructs were seeded into 10cm-dishes. Cells were stimulated (or mock treated) with 1000 U/mL IFNα2 for 16 h prior to addition of 500 μM biotin (Sigma-Aldrich) for 15 min at 37°C. Cells were then transferred to 4°C, washed five times with PBS, and lysed for 15 min in RIPA buffer supplemented with cOmplete Mini Protease Inhibitors (Roche) and PhosSTOP (Roche). Cells were sonicated to shear nucleic acids and lysates were cleared by centrifugation at 16,000 g for 15 min at 4°C. A fraction was taken and lysed in Laemmli buffer to represent total lysate. The remainder of the cleared sample was incubated with streptavidin-coated magnetic beads (Pierce Thermo Fisher) for 1 h at room temperature, or overnight at 4°C, on a rotator to allow binding of biotinylated proteins. Subsequently, samples were washed twice with RIPA buffer, once with 1 M KCl, once with 0.1 M Na_2CO_3, and once in freshly prepared 1 M urea in 10 mM Tris-HCl (pH 8.0). For western blot analysis, samples were washed two times in RIPA buffer and then eluted in Laemmli buffer. For proteomic analysis, samples were washed two times in freshly prepared 50 mM ammonium bicarbonate (NH_4HCO_3) and then eluted in the same buffer for liquid chromatography-mass spectrometry analysis performed by the Functional Genomics Center Zurich as previously described (Borold et al., 2021). The SaintExpress algorithm was used on the CRAPome website to analyze the MS data. The mass spectrometry proteomics data have been deposited to the ProteomeXchange Consortium via the PRIDE (Perez-Riverol et al., 2019) partner repository with the dataset identifier PXD029960.

QUANTIFICATION AND STATISTICAL ANALYSIS

Colocalization quantification using Imaris

Imaris software (version 9.7.2, Oxford Instruments) was used to quantify colocalizations between a viral marker (HA) and a component of the endosomal pathway (EEA1) from immunofluorescence images. The shortest distance to spots was utilized to define object-based colocalization between red spots (representing endo-lysosomal vesicles) and green spots (representing staining of viral proteins).

MFI quantification using ImageJ

For the indicated quantitative analyses, the mean fluorescence intensity (MFI) from immunofluorescence images was measured using ImageJ software (National Institutes of Health, Bethesda, USA).

Statistical analysis

Statistical analyses were performed using GraphPad Prism 9.1.2 (GraphPad Software, San Diego, California USA; https://www.graphpad.com/). Viral titer data and reporter assay data were log transformed and analyzed by unpaired one-way ANOVA for multiple comparisons. For quantifications of immunofluorescence signals, an unpaired nonparametric t test was used to compare different cell lines. For quantifications of colocalizations an unpaired nonparametric t test was used to compare two different cell lines and an ordinary two-way ANOVA was used to compare three different cell lines. Unpaired one-way ANOVA for multiple comparisons was used for analyzing normalized data. Specific statistical details of each experiment, and p values for significance, can be found in the appropriate figure legends.